South Asian Summer Monsoon and the Eastern Mediterranean Climate: The Monsoon–Desert Mechanism in CMIP5 Simulations

ANNALISA CHERCHI

Centro Euro-Mediterraneo sui Cambiamenti Climatici, and Istituto Nazionale di Geofisica e Vulcanologia, Bologna, Italy

H. ANNAMALAI

International Pacific Research Center, University of Hawai'i at Mānoa, Honolulu, Hawaii

SIMONA MASINA AND ANTONIO NAVARRA

Centro Euro-Mediterraneo sui Cambiamenti Climatici, and Istituto Nazionale di Geofisica e Vulcanologia, Bologna, Italy

(Manuscript received 29 August 2013, in final form 13 May 2014)

ABSTRACT

Dry summers over the eastern Mediterranean are characterized by strong descent anchored by long Rossby waves, which are forced by diabatic heating associated with summer monsoon rainfall over South Asia. The large-scale teleconnection between rising and subsiding air masses is referred to as the ''monsoon–desert mechanism.'' This study evaluates the ability of the phase 5 of the Coupled Model Intercomparison Project (CMIP5) models in representing the physical processes involved in this mechanism.

An evaluation of statistics between summer climatologies of monsoon diabatic heating and that of vertical velocity over the eastern Mediterranean suggests a linear relationship. Despite large spatial diversity in monsoon heating, descent over the Mediterranean is coherently located and realistic in intensity. To measure the sensitivity of descent to the diversity in the horizontal and vertical distribution of monsoon heating, a series of linear atmosphere model experiments are performed. It is shown that column-integrated heating over both the Bay of Bengal and the Arabian Sea provides the largest descent with a more realistic spatial pattern. In the vertical, CMIP5 models underestimate the diabatic heating at upper levels, while they overestimate it at lower levels, resulting in a weaker forced response and weaker associated descent over the Mediterranean. A moist static energy budget analysis applied to CMIP5 suggests that most models capture the dominant role of horizontal temperature advection and radiative fluxes in balancing descent over the Mediterranean. Based on the objective analysis herein, a subset of models is identified that captures the teleconnection for reasons consistent with observations. The recognized processes vary at interannual time scales as well, with imprints of severe weak/strong monsoons noticeable over the Mediterranean.

1. Introduction

a. Background

The Mediterranean sector (30°–50°N, 20°W–60°E) lies in a transition zone between the arid climate of North Africa and the wet climate of central Europe. The transition zone climate is influenced by interactions between midlatitude and tropical processes (Raicich et al. 2003; Giorgi and Lionello 2008). The region also has a complex topography and land surface phenology that modulates the climate at finer spatial scales (e.g., Lionello et al. 2006). In boreal summer [June through August (JJA)] the region is characterized by descending motion, northerly surface wind, and mostly westerlies in the middle troposphere (Raicich et al. 2003). Surface pressures are relatively high in the west, whereas in the east the Persian trough, which extends westward from the Asian monsoon, dominates the lower levels (Ziv et al. 2004). The described circulation corresponds to moisture divergence out of the Mediterranean and a minimum in seasonal rainfall (Mariotti et al. 2002).

In boreal summer, subsidence over the eastern Mediterranean (mostly east of 15°E) has been related to the tropical monsoon southeastward (Hoskins 1996;

Corresponding author address: Annalisa Cherchi, CMCC–INGV, Viale Aldo Moro 44, 40127 Bologna, Italy.
E-mail: annalisa.cherchi@bo.ingv.it

DOI: 10.1175/JCLI-D-13-00530.1

Rodwell and Hoskins 1996, hereinafter RH96) similar to other subtropical regions, such as California and Chile (Rodwell and Hoskins 2001, hereinafter RH01). In this theory, descent over the Mediterranean is a consequence of the interaction between westward propagating Rossby waves, which are generated by the diabatic heating associated with the summer monsoon rainfall in South Asia, and the mean westerly flow north of the region. These interactions are often referred to as the ''monsoon–desert mechanism.'' By recognizing the importance of horizontal temperature advection to balance the thermodynamic energy equation in midlatitudes, Rodwell and Hoskins employed an idealized model and demonstrated that the adiabatic descent is mainly of midlatitude origin (RH96). They also demonstrated the crucial importance of orography in determining the location of the descent: they showed how the terrain west of the descent is more effective than the orography in the east in delimiting the descent region (RH96).

In a subsequent paper (RH01), Rodwell and Hoskins emphasized the importance of local diabatic enhancement, primarily through radiative cooling, in strengthening the descent. Recently, Tyrlis et al. (2013) examined the monsoon–desert mechanism in atmospheric reanalysis products, finding that both subsidence and the northerly flow over the eastern Mediterranean and the Middle East are manifestations of the Rossby wave structure triggered by the monsoon convection. Other factors such as local albedo (Charney 1975) and the West African monsoon (Raicich et al. 2003; Gaetani et al. 2011) may also contribute to descent over the eastern Mediterranean region. In literature, the theory has been extended to the dynamics of the subtropical anticyclones in general, documenting, for example, the contribution from local air–sea interactions and the potential vorticity–potential temperature perspective (Chen et al. 2001; Seager et al. 2003; Liu et al. 2004; Nakamura and Miyasaka 2004).

b. *Present study*

Given the consensus that Asian monsoon heating is largely responsible for the summertime descent and dryness over the Mediterranean, and that large-scale processes are expected to be well resolved in coupled models, we attempt to diagnose the monsoon–desert mechanism using physically based tools with the objective to verify if the coupled models participating in the phase 5 of the Coupled Model Intercomparison Project (CMIP5) are able to represent the teleconnection for correct reasons. To the best of our knowledge, no previous studies have isolated this mechanism in general circulation models. In this analysis we adopt a three-step approach.

First, summer mean quantities of variables that are deemed important in the mechanism are diagnosed to assess the relationship from a statistical point of view. This approach is intended to provide guidance on the models' ability in capturing the teleconnection between monsoon heating and descent over the Mediterranean. Second, with the knowledge gained from these diagnostics, we perform a series of idealized experiments with a primitive equation linear atmosphere model. The idea and setup of the experiments follow from the awareness of the large diversity in the simulated latitudinal position and intensity of monsoon rainfall (Sperber et al. 2013), as well as from theoretical evidence suggesting that three-dimensional atmospheric circulation is sensitive to the structure and intensity of the vertical distribution of diabatic heating (Wu et al. 2000; Hoskins and Wang 2006; Liu et al. 2004). Third, considering that idealized modeling studies of RH96 and RH01 identified horizontal temperature advection and local radiative effects as dominant physical processes maintaining the descent over the Mediterranean, and recognizing the fact that temperature, radiative, and possibly moist processes are all involved, we applied moist static energy (MSE) budget analysis on CMIP5 historical simulations to quantify their relative roles. The additive value of using MSE budget rather the thermodynamic energy budget, as for example in Tyrlis et al. (2013), is that the former allows consideration of moisture, temperature, and radiative processes all together, taking into account also the interaction between moist convection and the circulation (see also Chou and Neelin 2003; Neelin 2007; Chen and Bordoni 2014a). To verify the leading mechanisms identified in the models, we examine the budget terms in the 40-yr European Centre for Medium-Range Weather Forecasts (ECMWF) Re-Analysis (ERA-40; Uppala et al. 2005). We note that the terms of the MSE budget encapsulate important physical parameterizations employed in numerical models and therefore it is an efficient diagnostic tool to isolate mechanisms and to understand models' strengths and weaknesses (Annamalai et al. 2013).

We will address the following questions in our analysis: To what degree does the diversity in the spatial distribution of monsoon rainfall impact the intensity of descent over the Mediterranean? In CMIP5 models considerable spread in the vertical distribution of diabatic heating is expected, given their diversity in the physical parameterizations: How do such variations influence the intensity and location of absolute descent over the Mediterranean? Do CMIP5 models represent horizontal temperature advection and local radiative effects adequately? Apart from temperature advection, does dry air injection from midlatitudes amplify the

descent? Finally, at interannual time scales do the large swings in South Asian monsoon rainfall (severe droughts or floods) influence the summer climate variations over the Mediterranean region? To the best of our knowledge, no past studies, either in observations or models, have addressed this question. We will investigate this aspect in CMIP5 historical simulations and observations, and evaluate MSE budget terms. Results from the present research are expected to pave the ground for further research exploring the future projections of the Mediterranean summer climate and its variations.

The remainder of the manuscript is organized as follows: Section 2 describes the models and the experimental design. Section 3 discusses the CMIP5 representation of the monsoon–desert mechanism in the time mean, followed by the analysis of the linear atmosphere model solutions. Section 4 is devoted to results at interannual time scales. Section 5 provides a summary and discussion of the implications of the present research.

2. Description of models, observations, methodology, and experiments

a. *Models and experiments*

1) CMIP5

The World Climate Research Program CMIP5 database provides multicentury-long simulations of the state-of-the-art global coupled models (Taylor et al. 2012). This comprehensive database offers a unique opportunity to assess the models' ability in representing the monsoon–desert mechanism and suggestions for model improvements. Here, we diagnose monthly mean fields from the historical simulations for the period 1901–2004 (Taylor et al. 2012). Some details of the models diagnosed, as well as expansions of model names, are listed in Table 1. For models with more than one member available, we computed the ensemble mean.

2) LINEAR BAROCLINIC ATMOSPHERE MODEL

The linear model used here is a global, time-dependent, primitive equation model (Watanabe and Kimoto 2000). It has a horizontal resolution at triangular truncation T21 and 20 vertical sigma (σ) levels. Because it has multiple levels it is referred as linear baroclinic model (LBM). To incorporate diffusion processes, Rayleigh friction and Newtonian damping are employed with a time scale varying with the vertical sigma levels. More details of the LBM and its configuration are available in Watanabe and Jin (2002).

To underscore the sensitivity of the summer climate subsidence over the eastern Mediterranean (Fig. 1) to the position and intensity of monsoon rainfall over South Asia (see Fig. 5) as well as to the vertical distribution of diabatic heating (see Fig. 8), as derived from CMIP5 model results, we conducted two set of experiments with the LBM. In the first set, we designed four experiments to account for the differences in the shape and intensity of the heating over South Asia, while in the second set we designed three experiments to account for the differences in the shape and intensity of the vertical profile of the heating. In both cases, the shape and intensity of the applied forcing are inspired by the CMIP5 models' performance (see Figs. 5 and 8).

3) EL NIÑO SENSITIVITY EXPERIMENTS

With the twofold aim to relate monsoon rainfall variations to extreme conditions over the Mediterranean, and to confirm that the leading processes identified in the summer mean climate are at work at interannual time scales, we diagnose an existing ensemble experiment conducted with the Geophysical Fluid Dynamics Laboratory (GFDL) atmosphere general circulation model, version 2.1 (AM2.1; Anderson et al. 2004). AM2.1 has a finite volume dynamical core with 24 vertical levels and a horizontal resolution of $2.5° \times 2.0°$. The 25-member analyzed ensemble was forced by composite El Niño–related SST anomaly patterns over the tropical Pacific during severe weak monsoons over South Asia, which are identified in long integrations of the companion GFDL coupled model version 2.1. (CM2.1; Delworth et al. 2006). CM2.1 consists of AM2.1 coupled to the Modular Ocean Model (MOM) version 4 with 50 vertical levels and a $1° \times 1°$ horizontal resolution (with a refinement around the equator). The experiments are conducted for the period 1 March–30 November and the members differ only in their initial conditions. More details about the experimental set up and the model's ability in capturing the El Niño–Southern Oscillation (ENSO)–monsoon teleconnection are available in Pillai and Annamalai (2012).

b. *Observations/reanalysis*

The model results have been compared with observations and reanalysis data. Precipitation fields are taken from two compilations: the Global Precipitation Climatology Project (GPCP) version 2.2 (Adler et al. 2003) at 2.5° resolution for the period 1979–2005 and the Climate Research Unit (CRU; Mitchell and Jones 2005) at 0.5° horizontal resolution for the period 1901–2005. Other atmospheric fields come from the ERA-40 reanalysis at 2.5° resolution for the period 1958–2001 (Uppala et al. 2005). The temporal resolution of precipitation and other atmospheric fields is monthly mean. (Only in Figs. 6b and 6c, the climatologies are computed from pentad values available from GPCP; Xie et al. 2003.)

TABLE 1. List and basic characteristics of the CMIP5 coupled models used.

Model name	Institute/country	Resolution (atmosphere/ocean)	Ensemble size
Australian Community Climate and Earth-System Simulator, version 1.3 (ACCESS1.3)	Commonwealth Scientific and Industrial Research Organisation (CSIRO) and Bureau of Meteorology (BOM)/Australia	1.875° × 1.25°/1.0° × 0.6°	1
Beijing Climate Center (BCC), Climate System Model, version 1.1 (BCC-CSM1.1)	BCC/China	2.8125° × 2.8125°/1.0° × 1.33°	1
Community Climate System Model, version 4 (CCSM4)	National Center for Atmospheric Research (NCAR)/United States	1.25° × 0.9°/1.1° × 0.54°	6
Community Earth System Model, version 1 with Community Atmosphere Model, version 5 (CESM1-CAM5)	NCAR/United States	1.25° × 0.9425°/1.125° × 0.47°	3
Centro Euro-Mediterraneo sui Cambiamenti Climatici (CMCC) Climate Model (CMCC-CM)	CMCC/Italy	0.75° × 0.75°/2.0° × 2.0°	1
CMCC Climate Model with a resolved stratosphere (CMCC-CMS)	CMCC/Italy	1.875° × 1.85°/2.0° × 2.0°	1
Commonwealth Scientific and Industrial Research Organisation (CSIRO) Mark, version 3.6.0 (CSIRO Mk3.6.0)	CSIRO and Queensland Climate Change Centre of Excellence (QCCCE)/Australia	1.875° × 1.875°/1.875° × 0.95°	9
Flexible Global Ocean–Atmosphere–Land System Model gridpoint, version 2 (FGOALS-g2)	State Key Laboratory of Numerical Modeling for Atmospheric Sciences and Geophysical Fluid Dynamics (LASG)/China	2.8125° × 3.06°/1.0° × 0.9°	1
Geophysical Fluid Dynamics Laboratory (GFDL) Climate Model, version 3 (GFDL CM3)	National Oceanic and Atmospheric Administration (NOAA) GFDL/United States	2.5° × 2.0°/1.0° × 0.9°	4
GFDL Earth System Model with Generalized Ocean Layer Dynamics (GOLD) component (GFDL-ESM2G)	NOAA GFDL/United States	2.5° × 1.5°/1.0° × 0.86°	3
Hadley Centre Coupled Model, version 3 (HadCM3)	Met Office Hadley Centre (MOHC)/United Kingdom	3.75° × 2.5°/1.25° × 1.25°	9
Hadley Centre Global Environment Model, version 2–Atmosphere and Ocean (HadGEM2-AO)	MOHC/United Kingdom	1.875° × 1.25°/1.0° × 0.83°	1
Institute of Numerical Mathematics (INM) Coupled Model, version 4.0 (INM-CM4)	INM/Russia	2.0° × 1.5°/1.0° × 0.53°	1
L'Institut Pierre-Simon Laplace (IPSL) Coupled Model, version 5A, mid resolution (IPSL-CM5A-MR)	IPSL/France	2.5° × 1.27°/2.0° × 2.0°	1
Model for Interdisciplinary Research on Climate, version 5 (MIROC5)	MIROC/Japan	1.4° × 1.4°/1.4° × 0.8°	5
Model for Interdisciplinary Research on Climate, Earth System Model (MIROC-ESM)	MIROC/Japan	2.8125° × 2.8125°/1.4° × 0.93°	3
Max Planck Institute (MPI) Earth System Model, low resolution (MPI-ESM-LR)	Max Planck Institute for Meteorology (MPI-M)/Germany	1.875° × 1.85°/1.4° × 0.8°	3
Norwegian Earth System Model, version 1, intermediate resolution (NorESM1-M)	Norwegian Climate Center (NCC)/Norway	2.5° × 1.895°/0.93° × 0.56°	3

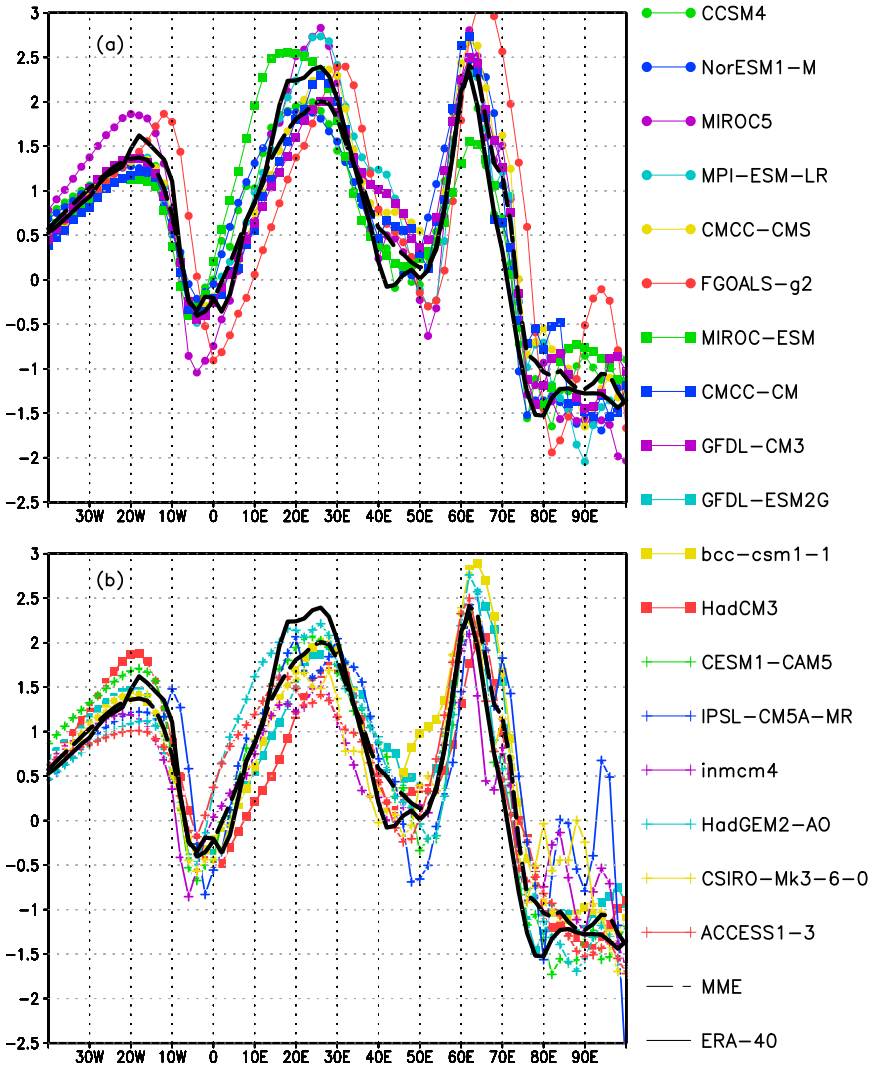

FIG. 1. JJA mean omega (hPa h^{-1}) at 500 hPa averaged over 28°–42°N. The values for ERA-40 (black solid line) and for the CMIP5 multimodel mean (black long-dashed line) are reported in both panels. Values for individual models (colored lines with marks; see legend) are distributed into two panels: (a) CCSM4, NorESM1-M, MIROC5, MPI-ESM-LR, CMCC-CMS, FGOALS-g2, MIROC-ESM, CMCC-CM, and GFDL CM3; and (b) GFDL-ESM2G, BCC-CSM1.1, HadCM3, CESM1-CAM5, IPSL-CM5A-MR, INM-CM4, HadGEM2-AO, CSIRO Mk3.6.0, and ACCESS1.3. (All model names are expanded in Table 1.)

Both reanalysis and CMIP5 models variables are interpolated on a common regular grid of 2° × 2° resolution for comparison. In the set of LBM experiments designed to test the influence of the horizontal shape and intensity of the heating over South Asia, a summer climatology for the period 1958–97 from the National Centers for Environmental Prediction (NCEP)-1 reanalysis (Kalnay et al. 1996) has been used as basic state.

c. *Diabatic heating*

The diabatic heating is computed as a residual of the thermodynamic energy equation, following the approach used by Hoskins et al. (1989) and Nigam et al. (2000). In particular, the three-dimensional form of the equation in pressure coordinates can be written as

$$\frac{\partial T}{\partial t} + \mathbf{v}\cdot\nabla T + \omega\frac{T}{\theta}\frac{\partial\theta}{\partial p} = \frac{J}{c_p}, \tag{1}$$

where T is temperature, $\mathbf{v}$ is the horizontal velocity vector, ω is vertical pressure velocity, θ is potential temperature, and c_p is specific heat at constant pressure. Also, J is the diabatic heating rate, and the term on the right-hand side of Eq. (1) is the diabatic heating at

pressure levels (Q_p). Applying the mass-weighted integral (i.e., $(1/g)\int dp$, where g is the acceleration due to gravity) to Eq. (1), the residual is the vertically integrated diabatic heating (Q_v). Because we are using monthly mean fields errors are expected in the computation of the diabatic heating as subseasonal and other shorter time scales variations do not emerge explicitly and are therefore included in the residual terms.

d. *Moist static energy budget*

To elucidate the leading processes in the mechanism, we apply moist static energy budget analysis following the approach described by Su and Neelin (2002) and Annamalai (2010). We must mention here that the MSE budget is not closed in reanalysis products (Back and Bretherton 2005; Kiranmayi and Maloney 2011; Prasanna and Annamalai 2012; Chen and Bordoni 2014a), nonlinear AGCM solutions (Pillai and Annamalai 2012), and fully coupled model integrations (Annamalai et al. 2013). The imbalance of the MSE budget may be ascribed to various reasons including space interpolation (MSE budget terms computed in common uniform grid instead of on original model grids, or on pressure levels instead of native sigma levels) and differences in the procedures for the computation of the advection terms. The temporal frequency of the fields considered here may also increase the residual term for all the transient terms that are not resolved in the analysis. Here, as described in sections 2a and 2b, we are using monthly mean data, consequently subseasonal and transient terms at shorter time scales do not emerge explicitly. Despite this shortcoming, MSE budget elucidates the leading mechanisms and offers pathways for model improvement.

The moist static energy, m, is given by

$$m = c_p T + gz + Lq, \tag{2}$$

where z is geopotential height, L is the latent heat of evaporation, q is the specific humidity, and the other terms are defined as in Eq. (1). The vertically integrated MSE tendency is given by

$$\left\langle \frac{\partial m}{\partial t} \right\rangle = -\langle \mathbf{v} \cdot \nabla m \rangle - \left\langle \omega \frac{\partial m}{\partial p} \right\rangle + F_{\text{rad}} + \text{LH} + \text{SH}, \tag{3}$$

where $\mathbf{v}$ is the horizontal velocity vector, ω is vertical pressure velocity, LH and SH are surface latent and sensible heat fluxes, respectively, and F_{rad} represents the net column-integrated radiative flux as a combination of longwave and shortwave heating rates. Angle brackets represent mass-weighted vertical integrals in the troposphere. All the terms in Eq. (3) are expressed in energy units (W m^{-2}).

The second term on the right-hand side of Eq. (3) represents the MSE divergence (or its vertical advection), while the first term is the horizontal advection of MSE. As the contribution from the horizontal advection of the potential energy is negligible, the horizontal advection of MSE can be decomposed into $-\langle \mathbf{v} \cdot \nabla Lq \rangle$ and $-\langle \mathbf{v} \cdot \nabla c_p T \rangle$ that correspond to the horizontal advections of latent energy and of dry enthalpy, respectively. The above considerations made our diagnostic equivalent to the budget analysis as applied in Chen and Bordoni (2014a).

In the analysis of the interannual variability, Eq. (3) is applied to the anomalous terms as

$$\left\langle \frac{\partial m}{\partial t} \right\rangle' = -\langle \mathbf{v} \cdot \nabla (c_p T) \rangle' - \langle \mathbf{v} \cdot \nabla (Lq) \rangle' - \left\langle \omega \frac{\partial m}{\partial p} \right\rangle' + F'_{\text{rad}} + \text{LH}' + \text{SH}', \tag{4}$$

where the prime ($'$) indicates strong or weak monsoon years composite anomaly. Extreme years are selected based on precipitation monsoon indices (see section 4 for more details), and the anomaly is computed with respect to summer mean seasonal climatology constructed from 103 years of historical simulations data for CMIP5 models (1901–2004) and 44 years for ERA-40 (1958–2001). Assuming steady-state at seasonal time scales the tendency term is negligible when estimating the climatology and the anomalies, and hence it is not explicitly included in the results shown in sections 3 and 4. Because of the importance of the horizontal temperature advection changes in the budget (Figs. 12 and 13, discussed later), the anomalous temperature advection term is partitioned as

$$\langle \mathbf{v} \cdot \nabla T \rangle' \sim \langle \mathbf{v}' \cdot \nabla T^c \rangle + \langle \mathbf{v}^c \cdot \nabla T' \rangle + \langle \mathbf{v}' \cdot \nabla T' \rangle, \tag{5}$$

where the prime and the superscript c indicate anomaly [as in Eq. (4)] and summer mean seasonal climatology, respectively. The first term, $\langle \mathbf{v}' \cdot \nabla T^c \rangle$, represents advection associated with anomalous wind acting on climatological temperature gradient. The second term, $\langle \mathbf{v}^c \cdot \nabla T' \rangle$, accounts for advection due to climatological wind acting on anomalous temperature gradient. The third term, $\langle \mathbf{v}' \cdot \nabla T' \rangle$, represents advection of anomalous wind acting on anomalous temperature gradient. Equation (5) has a residual term due to transient variability. It is primarily composed of intramonth and interannual transient eddies and it is very small (an order of magnitude smaller than the others). Indeed, transient eddy fluxes are small in most climate models (Chen and Bordoni 2014b).

3. The monsoon–desert mechanism in CMIP5 models

In this section, with simple diagnostics, we present the mechanism in the climatological features (section 3a),

followed by linear model solutions (section 3b) and detailed discussion of MSE budget analysis (section 3c).

a. Climatological features

In CMIP5 models, we begin our analysis by examining diabatic monsoon heating and descent over the Mediterranean region. Figure 1 shows summer mean (JJA) omega at 500 hPa averaged over 28°–42°N. Results from reanalysis (thick black line) show three local maxima in descent between the longitudes 40°W and 100°E: 1) the Atlantic Ocean (west of Greenwich), 2) the eastern Mediterranean sector (10°–40°E), and 3) western Asia (50°–70°E). Of the three, absolute descent occupies an extended area over the Mediterranean sector with maximum amplitude of about 2.5 hPa h^{-1}. Distinct subsidence maxima in the eastern Mediterranean and western Asia sectors are ultimately associated with the pronounced topography of the region (Tyrlis et al. 2013).

These regions of local maxima are realistically reproduced in the multimodel mean (Fig. 1, black long-dashed line), but compared to reanalysis the amplitude over the Mediterranean region is weaker by about 0.5 hPa h^{-1}. Individual models (Fig. 1, denoted by colored lines with symbols) have a wide spread of performances in reproducing these peak descents. Over the Mediterranean the models differ primarily in terms of intensity (the range of maximum amplitude lies between 1.4 and 2.9 hPa h^{-1}) but realistically reproduce longitudinal location of the maximum descent around latitudes 33°–35°N (not shown). The dispersion among models in terms of simulated intensity of the descent in western Asia is smaller compared to the eastern Mediterranean sector case, and this could be related with the relative larger impact of topography, which is comparably realistic in all models, in shaping the descent there. In both reanalysis and model results, ascent around 80°–90°E represents orographic rainfall along the Himalayas/Tibet region.

Does the spread in descent intensity over the eastern Mediterranean sector depend on the intensity and location of diabatic heating over South Asia? Figure 2 shows vertically integrated diabatic heating (Q_v) averaged between 5° and 25°N. In the monsoon region Q_v is dominated by latent heating over deep convective areas. The longitudinal profile from reanalysis (Fig. 2, black solid line) depicts multiple local maxima representative of deep convection over the Arabian Sea (~75°E), Bay of Bengal (90°–100°E), Southeast Asia (110°–140°E), and tropical west Pacific (~150°E). The multimodel mean (Fig. 2, black long-dashed line) realistically captures the maxima over Bay of Bengal/Southeast Asia even though the intensity is much weaker than observed (about half of the observed intensity). The models are systematically weak in capturing the heating east of 130°E (Fig. 2, denoted by colored lines with symbols). Unlike the descent (Fig. 1), large spread in amplitude and longitudinal locations of Q_v maximum suggests the models' limitation in capturing important details of the monsoon (Sperber et al. 2013; Annamalai et al. 2014, unpublished manuscript). Despite this inherent problem, subsidence in the eastern Mediterranean region is coherent and realistic in space.

To quantify the association, Fig. 3 relates midtropospheric (500 hPa) summer mean omega over the eastern Mediterranean (28°–42°N, 15°–35°E) and Q_v over South Asia (5°–25°N, 60°–100°E) in terms of both area averages (Fig. 3a) and their corresponding pattern correlation with ERA-40 (Fig. 3b). Figure 3a implies a quasi-linear relationship between the intensities of Q_v over South Asia and omega over the eastern Mediterranean, while the pattern correlations are more clustered around the values of 0.8 for omega and of 0.7 for Q_v (Fig. 3b). A plausible interpretation is that the models that cluster around these values can be considered more realistic in representing the mechanism because they have spatial patterns of both South Asian monsoon heating and eastern Mediterranean descent with the largest correlation with the reanalysis. For instance, the MIROC-ESM model (green square symbol in Figs. 3a,b) has high intensities in Q_v over South Asia and omega over eastern Mediterranean (Fig. 3a) but has the least pattern correlation in Q_v with reanalysis (Fig. 3b). In other words, while the descent location in the model is in good agreement with the reanalysis, the location of Q_v is not. More discussions on this and related aspects are deferred to sections 3b and 3c.

RH96 showed that monsoon heating–forced Rossby waves interact with air on the southern flank of the midlatitude westerlies, causing it to descend. Specifically, along the 325-K isentropic surface the northerly component of the westerly flow crossing it, in addition to the west to east pressure gradient, gives descent. Following RH96 approach, Fig. 4a shows winds (along with the meridional component, shaded) and pressure levels at 325-K isentropic surfaces for the reanalysis. Over the Mediterranean sector, the northerly component of the meridional wind velocity maximizes in the descent region where the wind vectors cross 325-K isentropic pressure levels (Fig. 4a), consistent with RH96. The results are shown for CMIP5 models in Fig. 4b as the multimodel mean (MME). The MME underestimates the intensity of the wind and tends to have the 325-K isentropic surfaces higher (Fig. 4b). However, the cross-contour flow and the latitudinal extent of the northerlies clearly indicate subsidence over the eastern Mediterranean.

Is there an association between the strength of simulated descent (Figs. 1 and 3a) and midtropospheric

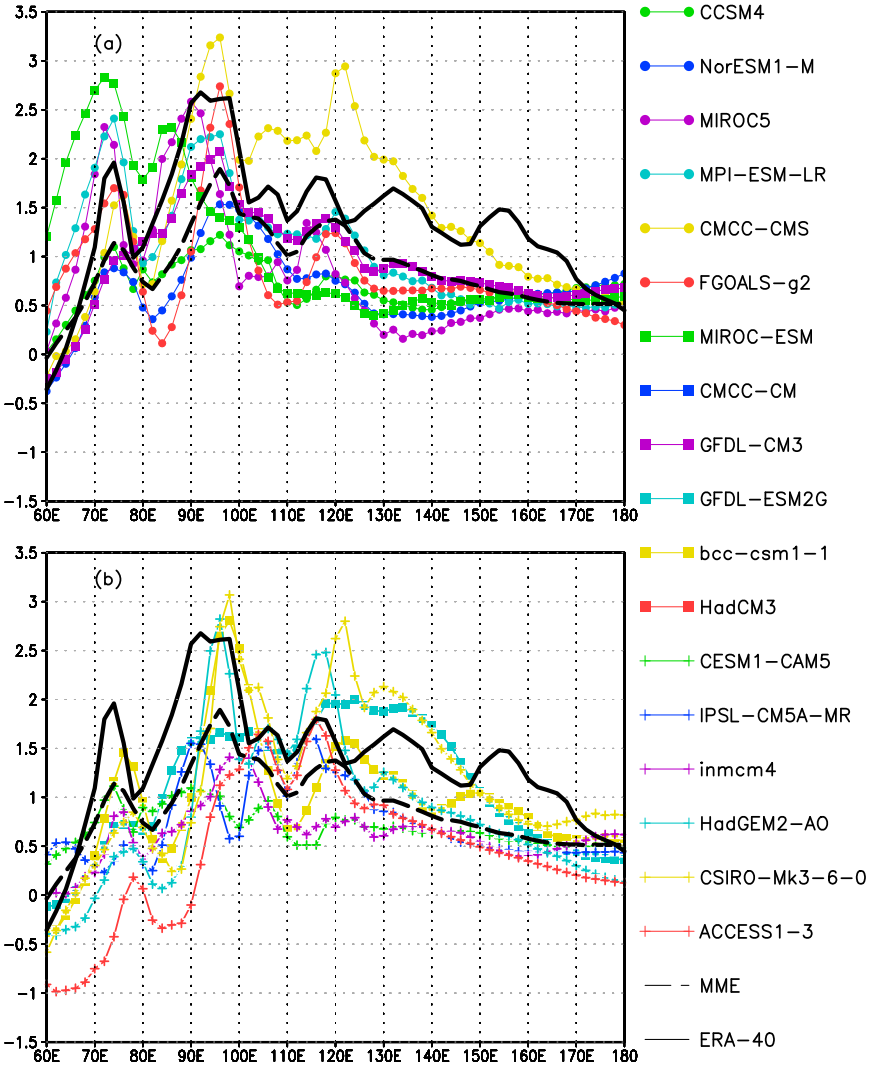

FIG. 2. As in Fig. 1, but for JJA mean vertically integrated diabatic heating (K day^{-1}) averaged over 5°–25°N.

westerlies/northerlies in the descent regions? In both reanalysis and models the 325-K isentropic surfaces are in the midtroposphere (not shown), so we can relate descent and meridional wind at 500 hPa. There is a quasi-linear relationship between the intensity of the descent averaged over 28°–42°N, 15°–35°E and the intensity of the 500-hPa meridional wind velocity averaged in the same region (Fig. 4c), with clustered model values around 2 hPa h^{-1} and -1.5 m s^{-1}, respectively. This association indicates that the models having the weakest descent also have the weakest northerly wind component in the midtroposphere. For example, the models ACCESS1.3 (Fig. 1, red line with crosses), CSIRO Mk3.6.0 (Fig. 1, yellow line with crosses), and INM-CM4 (Fig. 1, purple line with crosses) all depict very weak descent (~1.25 hPa h^{-1}) over the eastern Mediterranean and their simulated northerlies in the descent region are weaker by more than 40% (Fig. 4c, red, yellow, and purple diamond, respectively) compared to reanalysis. A similar behavior holds also for the zonal velocity component (not shown).

b. *Linear atmosphere model solutions*

Results presented above raise an important question: Among the models, despite a large diversity in the simulated Q_v over South Asia (Fig. 2), why is the descent over the Mediterranean coherent (Fig. 1)? The answer to this question is a valuable point in the understanding of the simulated mechanism given, for example, the strong descent but very weak pattern correlation in Q_v in the case of MIROC-ESM model (Fig. 3).

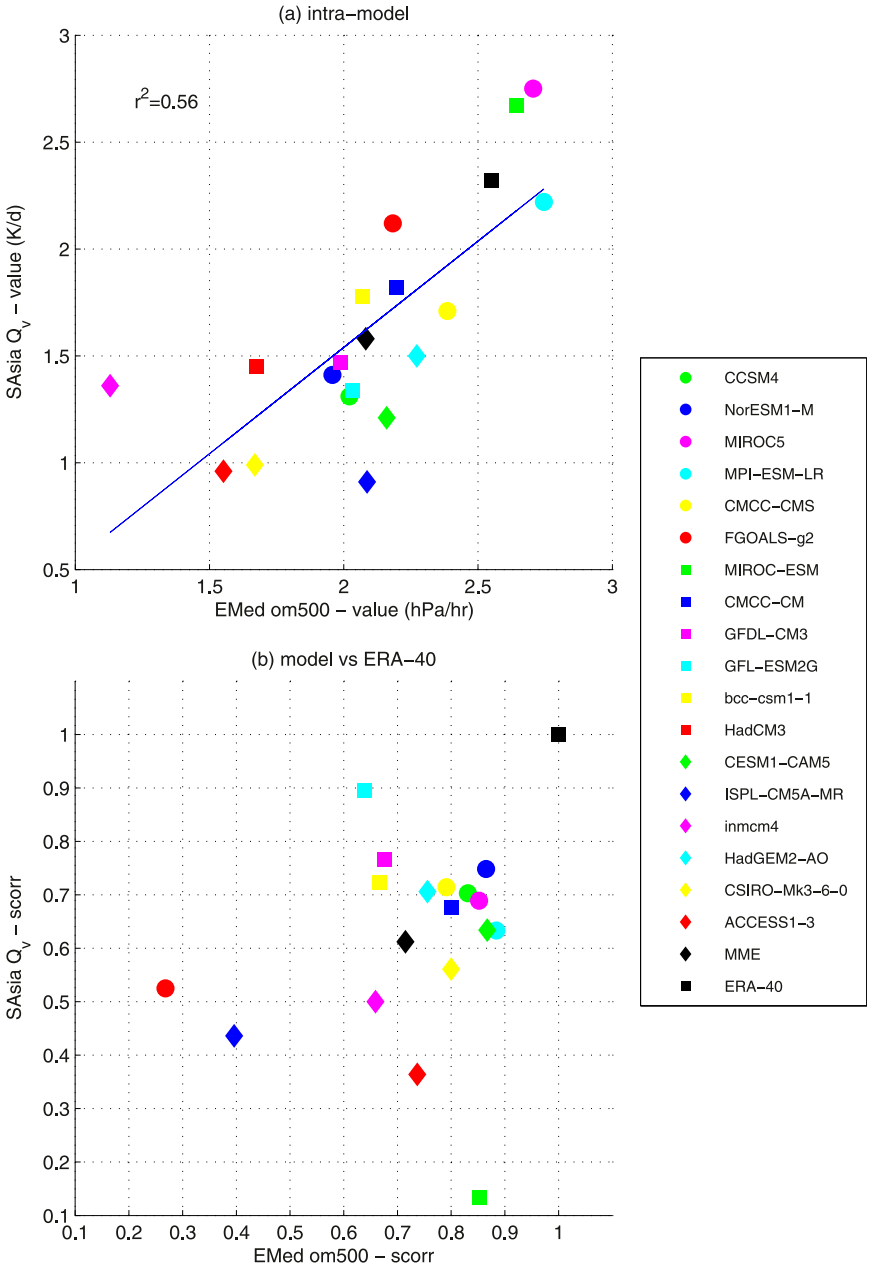

FIG. 3. Scatterplots of JJA mean omega at 500 hPa (om500) in the eastern Mediterranean area (EMed; 28°–42°N, 15°–35°E) and of vertically integrated diabatic heating (Q_v) over South Asia (5°–25°N, 60°–100°E) in terms of (a) area-averaged values (hPa h^{-1} and K day^{-1}, respectively) and (b) centered pattern correlation with the same fields computed from ERA-40. The blue solid line in (a) corresponds to the linear best fit, and the coefficient of determination (r^2) is in the top-left corner of the panel.

1) SENSITIVITY TO THE SPATIAL PATTERN OF THE HEATING

The idealized modeling study of RH96 implied that maximum descent over the Mediterranean is accomplished if the prescribed maximum heating is centered over the Bay of Bengal (25°N, 90°E). Such an off-equatorial heat source is efficient to excite Rossby waves that interact with midlatitude westerlies to provide maximum subsidence.

Figure 5 shows summer rainfall climatology for CMIP5 models along with their multimodel mean and observations. It is clear that the position of maximum rainfall for a group of models is located over the Arabian

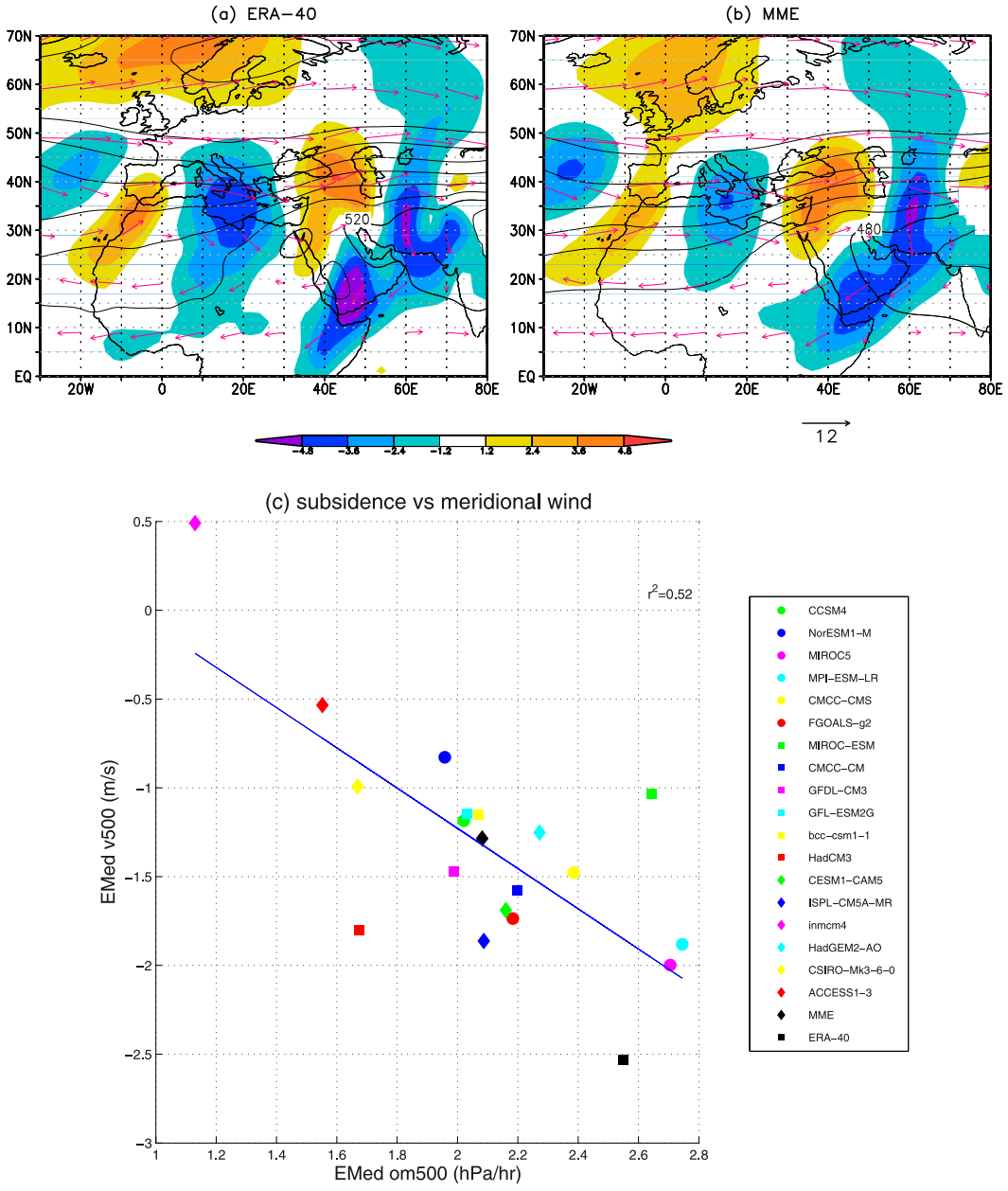

FIG. 4. JJA mean wind vectors (m s^{-1}, pink arrows), meridional wind velocity (m s^{-1}, shaded), and pressure levels (hPa, contours with 50-hPa contour interval) on isentropic surfaces at 325K for (a) ERA-40 and (b) the multimodel mean (MME). (c) Scatterplot of JJA mean omega (hPa h^{-1}) and of meridional wind velocity (m s^{-1}) at 500 hPa averaged over 28°–42°N, 15°–35°E. The blue solid line in (c) corresponds to the linear best fit, and the coefficient of determination (r^2) is in the top-right corner of the panel.

Sea (e.g., MIROC-ESM) or along the near-equatorial Indian Ocean (e.g., CSIRO Mk3.6.0) or over the plains of Southeast Asia (e.g., ACCESS1.3). The models' rainfall climatology patterns can be associated with different phases of "observed" monsoon (Figs. 6a–c). For example, in 6–15 May (or preonset phase; see also Ananthakrishnan et al. 1983) heaviest precipitation is localized around near-equatorial Indian Ocean (Fig. 6b). As the monsoon progresses in time, the rainfall maximum shifts to the northern Bay of Bengal and the Arabian Sea (Fig. 6c). At this stage—that is, during the established (5–14 Jun) monsoon phase (Ananthakrishnan et al. 1983)—the precipitation pattern is more similar to the summer mean (Fig. 6a). A cleaner way of addressing the

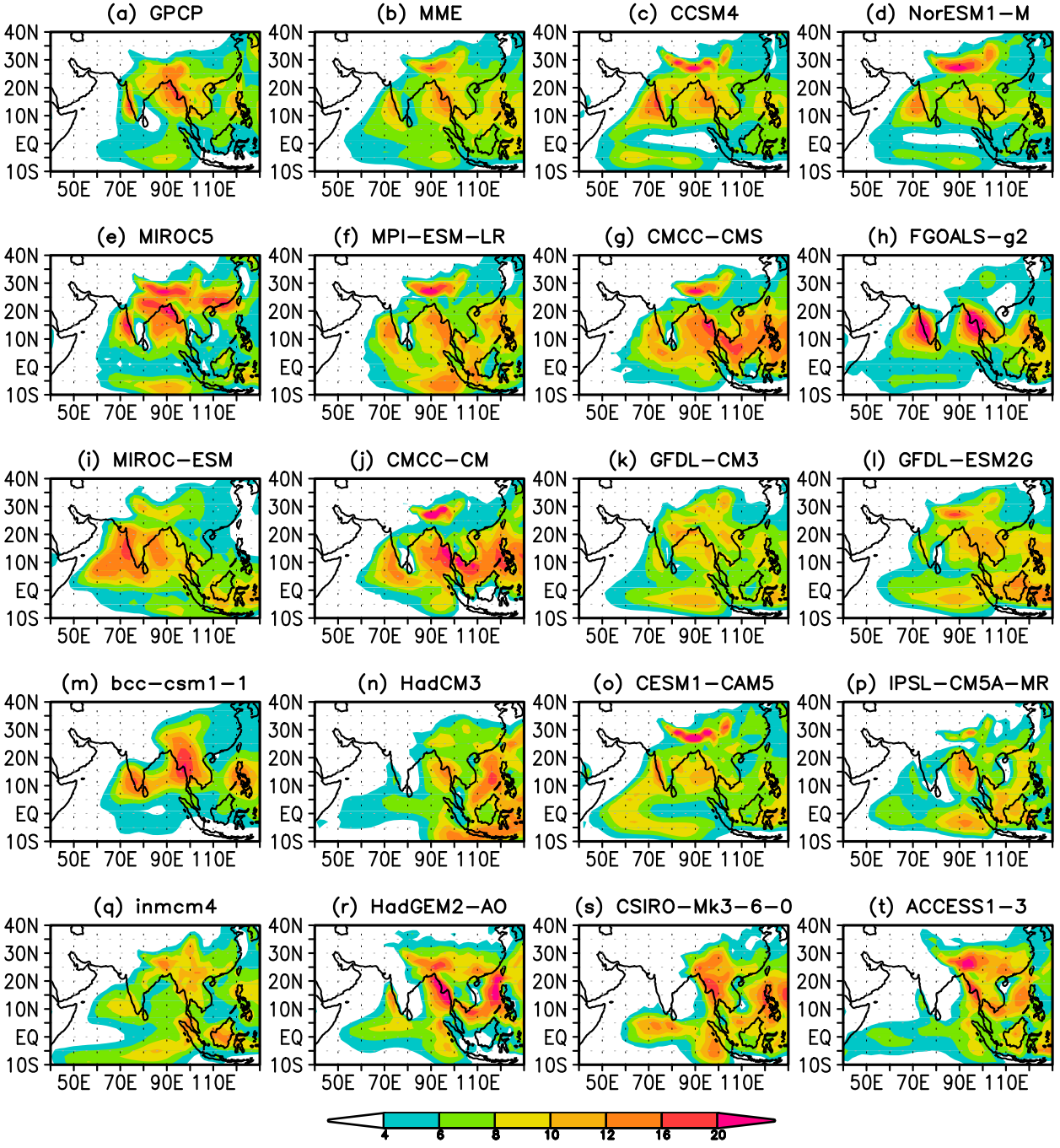

FIG. 5. JJA mean precipitation (mm day^{-1}) for (a) GPCP data, (b) CMIP5 multimodel mean, (c) CCSM4, (d) NorESM1-M, (e) MIROC5, (f) MPI-ESM-LR, (g) CMCC-CMS, (h) FGOALS-g2, (i) MIROC-ESM, (j) CMCC-CM, (k) GFDL CM3, (l) GFDL-ESM2G, (m) BCC-CSM1.1, (n) HadCM3, (o) CESM1-CAM5, (p) IPSL-CM5A-MR, (q) INM-CM4, (r) HadGEM2-AO, (s) CSIRO Mk3.6.0, and (t) ACCESS1.3.

questions raised above is to force the LBM with each and every CMIP5 model's simulated rainfall and linearize the equations around each model's basic state. To circumvent this laborious approach, given that the models' rainfall climatology can be associated with different phases of observed monsoon, we have followed a different approach.

To test the sensitivity in local rainfall maximum positions, we performed four experiments with prescribed heating patterns as shown in Figs. 6d–g. The forcing

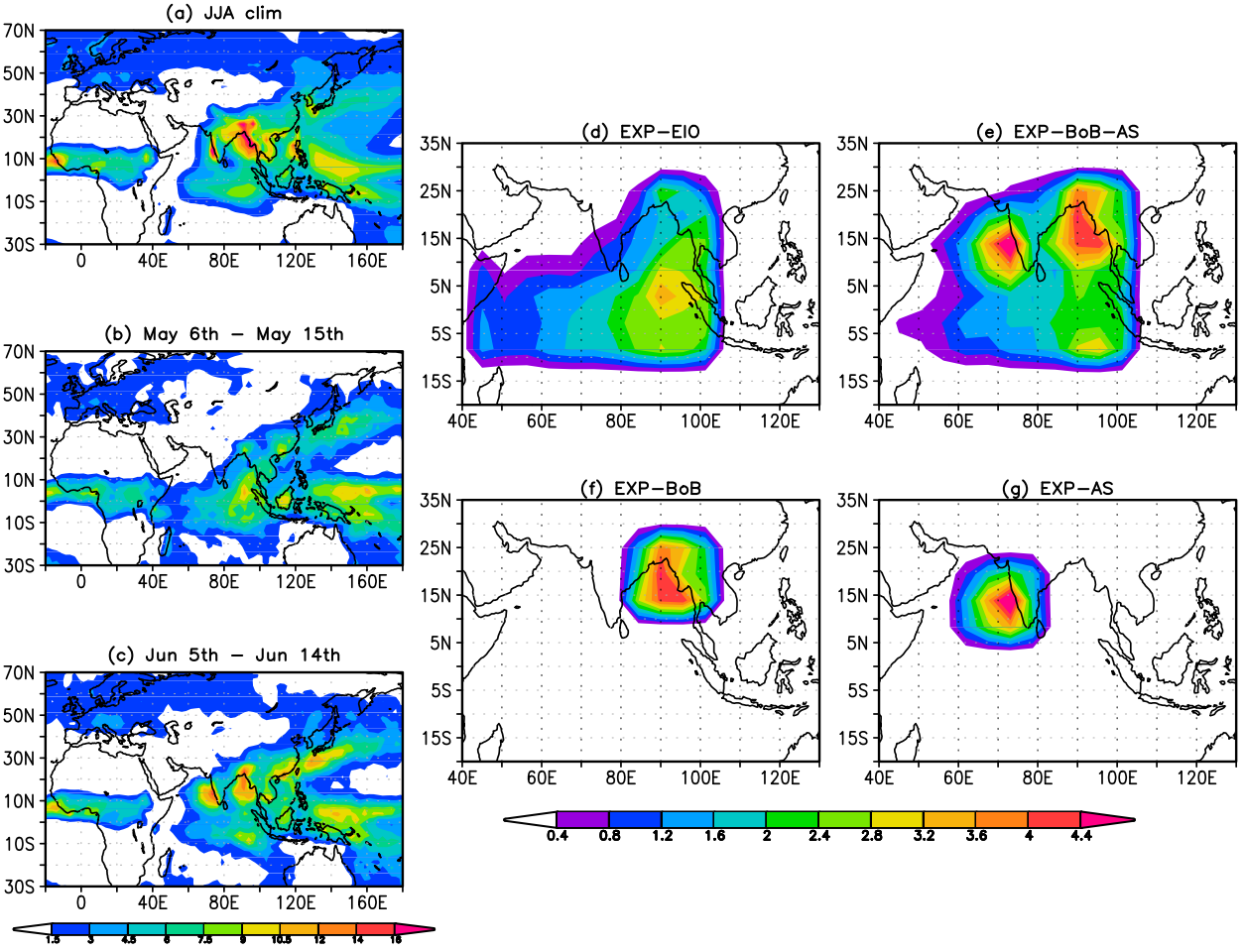

FIG. 6. Mean precipitation (mm day^{-1}) averaged in (a) JJA, (b) the preonset (6–15 May) and (c) the established (5–14 Jun) monsoon phases computed from GPCP dataset (climatologies from pentad means). Heating forcing (°C day^{-1}) applied in the LBM experiments (d) EXP-EIO, (e) EXP-BoB-AS, (f) EXP-BoB, and (g) EXP-AS.

mimics the preonset (Fig. 6d; EXP-EIO), established (Fig. 6e; EXP-BoB-AS), Bay of Bengal portion of the established (Fig. 6f; EXP-BoB), and Arabian Sea component of the established (Fig. 6g; EXP-AS) monsoon phases, respectively. In all experiments, LBM is linearized with basic state constructed from NCEP reanalysis (Kalnay et al. 1996). For EXP-EIO the basic state for the month of May is used, whereas for the other cases it is June. In all cases, the prescribed heating maximizes around 400 hPa and its vertical integral is equivalent to the amount of latent heating provided by the respective rainfall amount. In this set of experiments the vertical profile of the imposed forcing is similar to the profile of the EXP-IP described later (Fig. 9). As in Annamalai and Sperber (2005), the LBM was integrated for 30 days with fixed forcing, and the model reaches steady state after day 15.

The response in terms of anomalous subsidence is shown in Fig. 7. Irrespective of the maximum rainfall locations, the forced equatorially trapped long Rossby waves (i.e., those having small wavenumber and covering more rapidly long distances) interacting with the midlatitude westerlies are effective in anchoring the descent, and hence all the four solutions capture descent anomalies over the eastern Mediterranean. In this set of LBM experiments midtropospheric subsidence over western Asia is noted in the early stages of the solution, as part of the westward propagating Rossby waves, but the intensity is not sustained during the steady state (not shown), perhaps due to inadequate representation of local orography, as well as limitations in the interactions between Rossby waves and midlatitude westerlies.

The combined heating over the Arabian Sea/Bay of Bengal sector corresponds to the largest forcing in the four experiments considered and it exerts the largest descent over the eastern Mediterranean (Fig. 7b). Heating prescribed over the equatorial Indian Ocean (Fig. 7a) is also effective in promoting descent in the

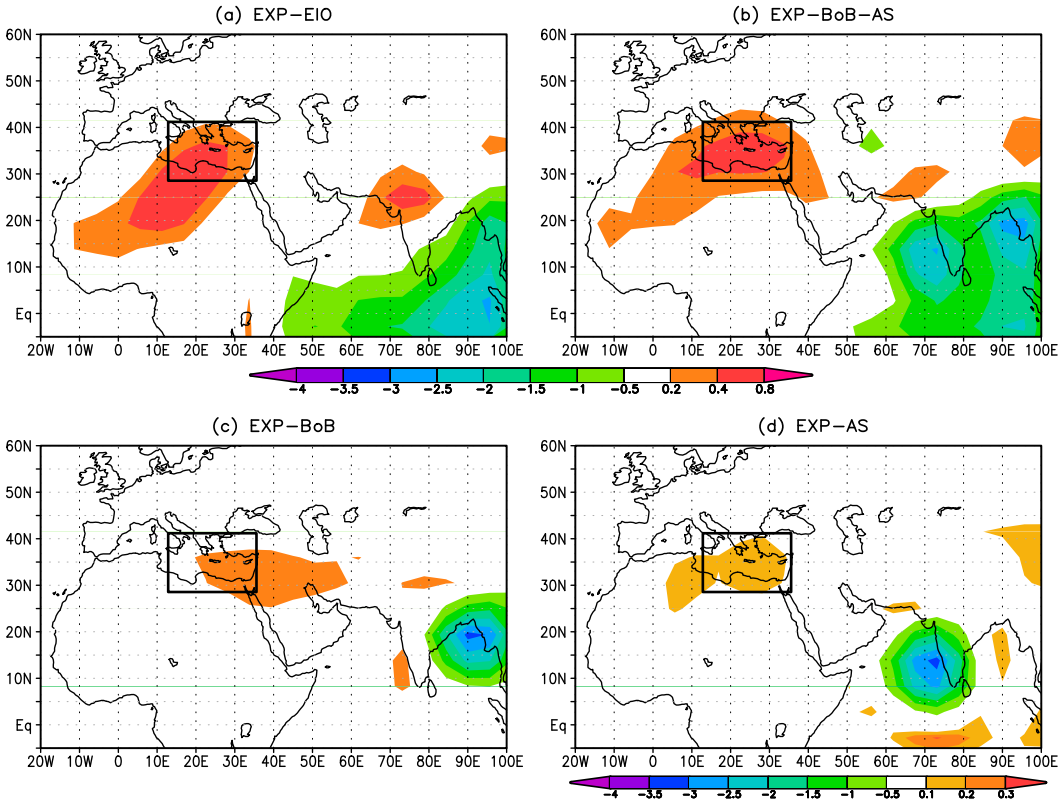

FIG. 7. Steady-state response (day 21) of anomalous omega at 500 hPa (hPa h^{-1}) in (a) EXP-EIO, (b) EXP-BoB-AS, (c) EXP-BoB, and (d) EXP-AS. The palette for (d), located just below the panel itself, differs from the palette for the other three panels, located in the middle of the figure, as the positive values of omega (yellow-red colors) are almost halved. A black rectangular box in each panel indicates the eastern Mediterranean sector as considered in our analysis.

eastern Mediterranean. As discussed in RH96, when the heating is at lower latitudes the Northern Hemisphere Rossby wave solution is weaker but the symmetric Kelvin mode is stronger. In the other two experiments, the heating over the Bay of Bengal and the Arabian Sea sectors has been separated. The results show that, of the two, the heating in the Bay of Bengal alone (Fig. 7c) forces a descent in the eastern Mediterranean that is about halved and more eastward if compared to the previous two experiments. When the heating is in the Arabian Sea only, there is descent in the eastern Mediterranean but its intensity is extremely weaker than in the other cases (Fig. 7d; note that the palette of this panel differs from that of the other panels as the intensity of the descent, shown in yellow–red colors, is more than halved). Including the Arabian Sea heating in conjunction with that over Bay of Bengal provides realistic subsidence in the eastern Mediterranean. Because of the coarse resolution of the LBM used [see section 2a(2)], other factors such as orography are compromised. Our LBM solutions and comparison with CMIP5 suggest that coherent descent in the eastern Mediterranean as noted in Fig. 1 is expected, despite the diversity in simulated monsoon rainfall (Fig. 5).

2) SENSITIVITY TO THE VERTICAL PROFILE OF THE HEATING

Figure 8 shows the vertical profile of diabatic heating Q_p averaged over the South Asian monsoon region (5°–25°N, 60°–100°E). As expected over deep convective regions, the profile from the reanalysis (black solid line) captures peak values around the midtroposphere (500–400 hPa). While many models tend to have maxima at midtroposphere, the simulated Q_p is higher than that in the reanalysis in the lower troposphere (900–700 hPa), but it is lower in the layer 700–300 hPa, a feature readily apparent in the multimodel mean (black long-dashed line). Some outliers such as CSIRO Mk3.6.0 and ACCESS1.3 do not show any appreciable vertical variations since they simulate very weak precipitation over Bay of Bengal/Arabian Sea sectors but higher and unrealistic precipitation over plains of Indo-China and East Asia (Figs. 5s,t). INM-CM4 and IPSL-CM5A-MR have similar weak vertical profiles (Fig. 8), but while the former

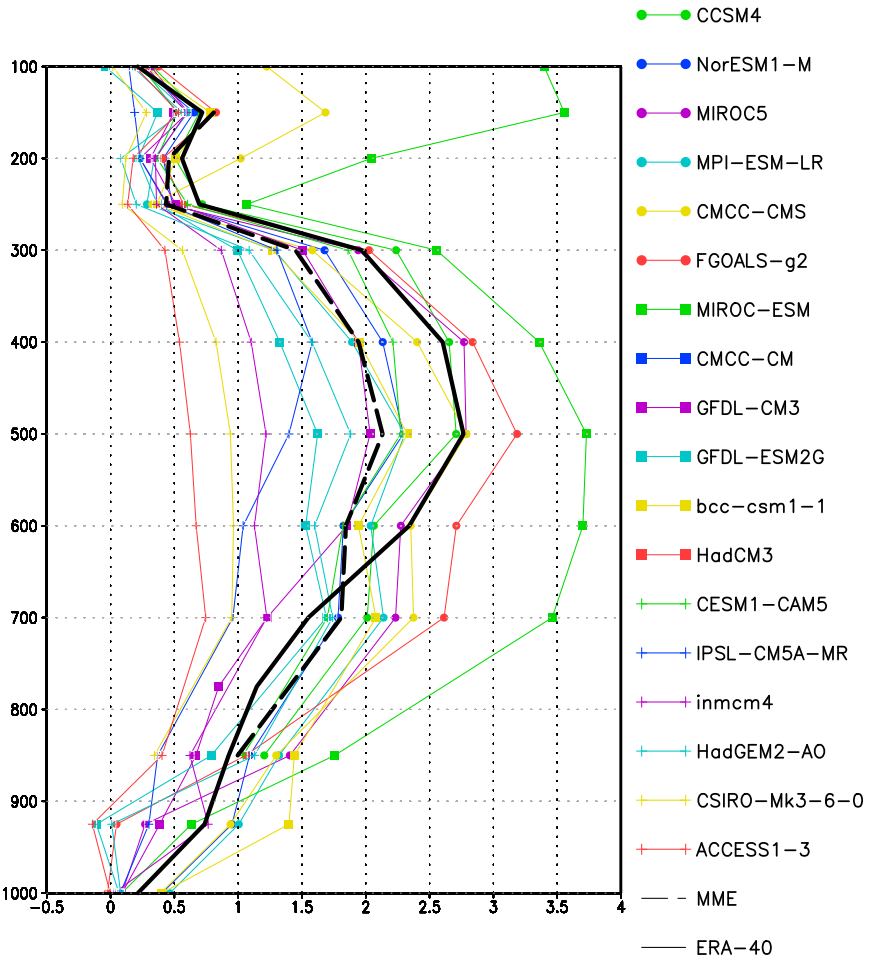

FIG. 8. Vertical profiles of JJA mean diabatic heating (K day^{-1}) averaged over Asia (5°–25°N, 60°–100°E) for ERA-40 (black solid line), the CMIP5 multimodel mean (black long-dashed line), and for the individual models (colored lines with marks; see legend).

has no gradients, the latter shows a local maximum around 400 hPa and stronger subsidence in the eastern Mediterranean (Fig. 1). If we consider the conclusions derived from the linear solutions previously discussed (Fig. 7), this difference is also consistent with the respective precipitation patterns—that is, more precipitation over the Bay of Bengal and over the equatorial Indian Ocean for IPSL-CM5A-MR (Fig. 5p) and more precipitation in the Arabian Sea for INM-CM4 (Fig. 5q).

Tropical Rainfall Measuring Mission (TRMM) observations indicate that over the monsoon region stratiform rainfall largely contributes to diabatic heating intensity (Schumacher et al. 2004). In the models the picture could be different. Most of the models participating in phase 3 of the Coupled Model Intercomparison Project (CMIP3) produce too much convective (~95% of the total) and too little stratiform precipitation (Dai 2006). The analysis by Sperber et al. (2013) suggests that there is little or no improvement in the simulation of monsoon precipitation climatology from CMIP3 to CMIP5. Figure 8 indicates that in the CMIP5 models over the monsoon region substantial latent heat is released at lower tropospheric levels, perhaps corresponding to shallow convection. Yet in most of the models the diabatic heating still peaks in the midtroposphere.

To understand circulation response to vertical gradients in the diabatic heating, we selected three profiles from the CMIP5 pool corresponding to "weak," "intermediate," and "strong" gradients (Fig. 9a). Models that belong to the weak Q_p-profile category are ACCESS1.3, CSIRO Mk3.6.0, INM-CM4, and IPSL-CM5A-MR (Fig. 8). MIROC-ESM and FGOALS-g2 are examples of models grouped in the strong category, while MIROC5, CCSM4, and CMCC-CMS belong to the intermediate Q_p profile group. We performed LBM experiments by imposing these profiles and linearizing the equations around the corresponding CMIP5 models'

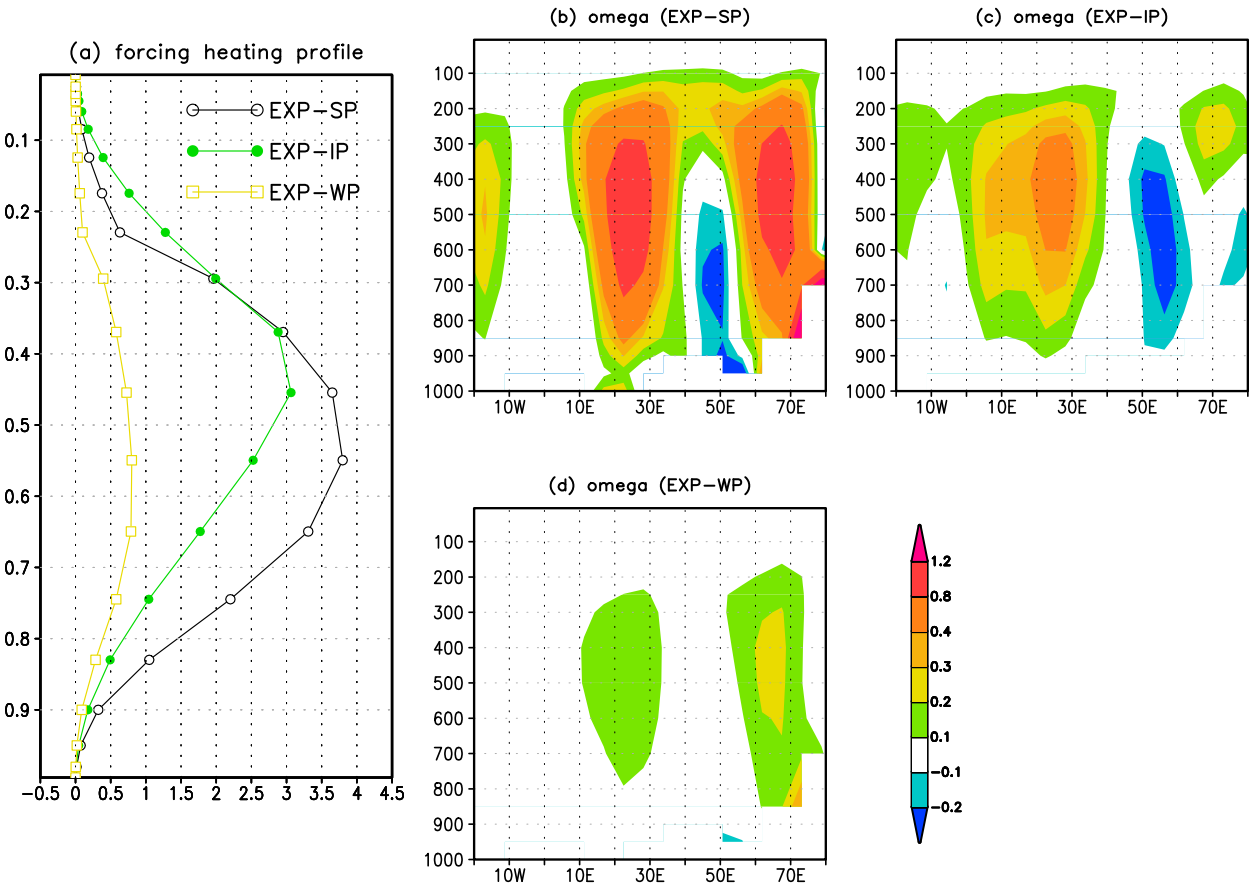

FIG. 9. LBM experiments (EXP-SP, EXP-NP, and EXP-WP): (a) vertical profiles of imposed heating forcing (°C day^{-1}) averaged over 5°–25°N, 60°–100°E; (b)–(d) steady-state response (day 21) of anomalous omega (hPa h^{-1}) averaged over 28°–42°N.

summer mean basic state. The experiments are named EXP-SP, EXP-IP, and EXP-WP and represent the strong, intermediate, and weak profile, respectively. Figures 9b–d show anomalous vertical cross sections of omega averaged over the descent latitudes (28°–42°N) at day 21 of the LBM experiments.

In all the experiments, the vertical velocity over the Mediterranean is proportional to the vertical profile of the imposed diabatic heating. The heating profile in EXP-IP is a reasonable approximation to that of ERA-40 (Fig. 8, solid black line). The model response (Fig. 9c) captures descent in all the three regions as noted in Fig. 1 with a local maximum over the eastern Mediterranean. As mentioned in previous subsection, the lack of adequate representation of orography in our coarse-resolution model may lead to a weaker response over western Asia. An examination of the temporal evolution of omega (not shown) suggests that descent over western Asia (~70°E) maximizes around day 6, while descent over the Mediterranean and over the Atlantic maximizes at day 11 and day 14, respectively. This time evolution agrees with the group velocity of Rossby waves in the Northern Hemisphere as discussed in RH96. In EXP-SP (Fig. 9b), the linear model response is strong because of the unrealistic and too strong (as compared to ERA-40) imposed profile. In contrast, in response of nearly uniform vertical diabatic heating in EXP-WP, the forced Rossby wave is weak and is largely confined to western Asia (Fig. 9d). In this case, the temporal evolution of the solution (not shown) suggests no appreciable amplitude of the long Rossby waves beyond western Asia.

These results are illustrative of the CMIP5 models' performance. In agreement with the results of EXP-WP, the models belonging to the weak Q_p-profile category all have very weak descent over the eastern Mediterranean but show realistic descent over western Asia (Fig. 1). Similarly, the models in the strong Q_p-profile category have stronger descent over the Mediterranean as well as over western Asia (Fig. 1). The intermediate category models have realistic descent over the Mediterranean (Fig. 1) but stronger than that descent suggested by LBM solutions over western Asia (Fig. 9c). Apart from the forced Rossby waves and their interaction with

midlatitude westerly winds, realistic representation of orography is important in capturing the local maxima in descent (RH96; Tyrlis et al. 2013; Boos and Hurley 2013). Here, due to the coarse horizontal resolution in LBM, the effect of orography may be compromised influencing the simulated descent.

c. *MSE budget analysis*

The above results imply the existence of a monsoon–desert mechanism in CMIP5 models. Given that result, in order to quantify the relative roles of temperature, moisture, and radiative processes in shaping the descent over the eastern Mediterranean we apply the MSE budget analysis [Eq. (3)] to the summer mean basic state for both ERA-40 reanalysis and all the CMIP5 models. Figure 10 shows the leading terms estimated from ERA-40. In all the three descent regions vertical advection of MSE (vertically integrated quantity) is negative (Fig. 10a), implying import of energy by the divergent circulation (as we are referring to descent regions, divergence occurs mainly at low levels). The MSE stratification in the atmosphere is negative, hence regions of positive (negative) vertical advection correspond to ascending (descending) vertical motion (see also Chen and Bordoni 2014a). In seeking balance, horizontal advection of dry enthalpy (Fig. 10b) overwhelms MSE divergence in all the three regions. The net radiative flux ($F_{\rm rad}$, Fig. 10d) identifies a local maximum (intense radiative cooling) over the eastern Mediterranean (28°–42°N, 15°–35°E), where it contributes to MSE divergence for about 30% (see Table 2). In particular, radiative cooling through promoting diabatic descent amplifies the adiabatic descent due to horizontal temperature advection ($T_{\rm adv}$). Descent can be also promoted by radiative cooling (Fig. 10d) balanced by adiabatic warming (Fig. 10e). The ratio between horizontal and vertical temperature advection (absolute value) defines the portion of adiabatic descent (RH01). Our results of horizontal and vertical temperature advection (Figs. 10b,e, as expressed in energy units) are in good agreement with those of Tyrlis et al. (2013).

In the Mediterranean region, the vertically integrated climatological moisture is slightly larger in the west than in the east (resulting in a west–east gradient, not shown), and is predominantly advected by the mean westerlies. In the budget, horizontal advection of latent energy (Fig. 10c) partially offsets the large negative values due to $F_{\rm rad}$ and horizontal advection of dry enthalpy. Latent and sensible heat fluxes are also positive in the area (Table 2). The values of the MSE budget terms for the models listed in Table 2 indicate a positive contribution from horizontal moisture advection and sensible and latent heat fluxes as well. Yet the budget both in reanalysis and CMIP5 models is not closed. The imbalance varies among the models, ranging from 10% to 30% (Table 2).

Over the eastern Mediterranean, reanalysis results indicate that $T_{\rm adv}$ and $F_{\rm rad}$ are two dominant terms of the MSE budget (Fig. 10 and Table 2). In CMIP5 models, these two terms are discussed in some details as area-averaged over the eastern Mediterranean (Fig. 11 and Table 2). If the contribution of horizontal temperature advection and radiative flux to MSE budget from reanalysis reflects a ''true'' value (Fig. 11c, black square), then most CMIP5 models underestimate the contribution of $T_{\rm adv}$ while they overestimate that of $F_{\rm rad}$ in their respective budgets (Fig. 11c). The actual amplitude of $T_{\rm adv}$ in models varies from about -0.2 to $-0.98\,{\rm K\,day^{-1}}$ with the reanalysis value being $-0.725\,{\rm K\,day^{-1}}$ (Fig. 11a). A near-linear relationship exists between $T_{\rm adv}$ and adiabatic descent, as defined above through the ratio between horizontal and vertical temperature advection (Fig. 11b). That relationship indicates that the largest intensity of horizontal temperature advection in the Mediterranean area corresponds to largest component of adiabatic descent. The models that have the weakest descent over the eastern Mediterranean (Fig. 1) and weakest diabatic heating with small vertical variations over South Asia (Fig. 8) also have the lowest $T_{\rm adv}$ and the highest $F_{\rm rad}$ values. Figure 11c evidences an unrealistic contribution by adiabatic processes to the budget, suggesting that in some models systematic errors in diabatic processes mask the monsoon–desert mechanism.

In summary, based on the suite of diagnostics shown in section 3a in conjunction with LBM solutions (section 3b) and MSE budget analysis (Fig. 11), not a single model stands out as ''best'' in capturing the monsoon–desert mechanism. While there are models that have realistic monsoon rainfall and vertical distribution of diabatic heating, the relative contributions of $T_{\rm adv}$ and $F_{\rm rad}$ to the MSE budget that determine descent intensity over the eastern Mediterranean differ considerably from those obtained from reanalysis. Within these constraints and combining the models' performance in representing the crucial parameters for the monsoon–desert mechanism (mostly summarized in the scatterplots, i.e., Figs. 3 and 11), we identify a few models, namely CCSM4, MIROC5, CMCC-CMS, GFDL CM3, MPI-ESM-LR, CMCC-CM, and CESM1-CAM5, that are capable of representing the teleconnection for the correct reasons. These few models satisfy many of its aspects, such as the latitudinal/longitudinal position of monsoon rainfall (Fig. 5) and associated vertical distribution of Q_p (Fig. 8), descent intensity over the eastern Mediterranean (Fig. 1), and related processes such as horizontal temperature advection and

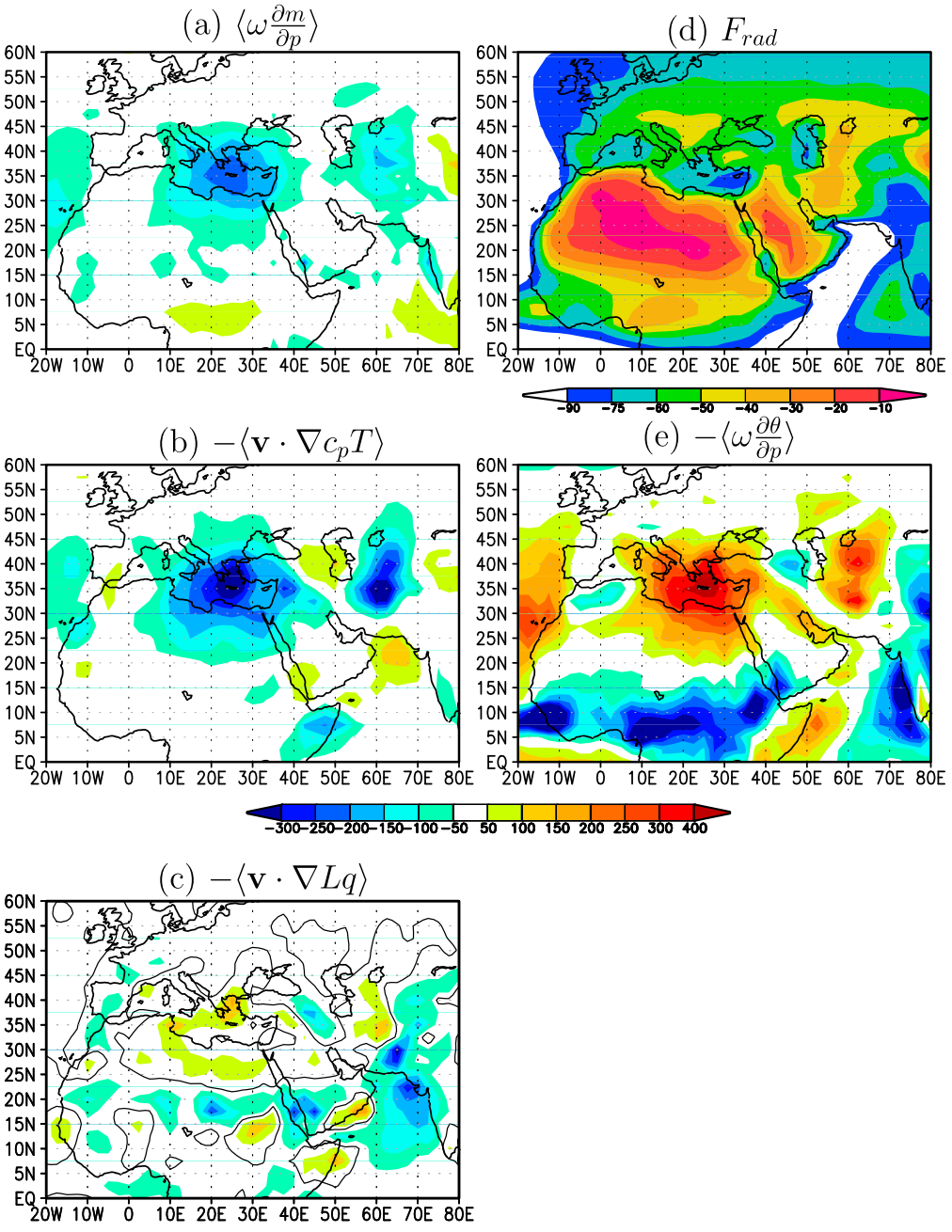

FIG. 10. JJA mean of (a) vertical advection of moist static energy ($\langle\omega(\partial m/\partial p)\rangle$), (b) horizontal advection of dry enthalpy ($-\langle\mathbf{v}\cdot\nabla c_pT\rangle$), (c) horizontal advection of latent energy ($-\langle\mathbf{v}\cdot\nabla Lq\rangle$, with the zero contour in black), and (d) the radiative flux ($F_{\rm rad}$) from the MSE budget [Eq. (3)]; (e) the vertical temperature advection. All the fields are mass-weighted vertical integrals from the ground to about 100 hPa and are measured in W m^{-2}. Note that (d) has a separate palette located just below it, while all the other panels share the palette located in the middle of the figure.

net radiative flux (Fig. 11). Here we have not considered MIROC-ESM despite its realistic representation of the processes primarily because of its unrealistic monsoon rainfall simulation over the western Arabian Sea (Fig. 5i), resulting in a very poor pattern correlation in Q_v (Fig. 3b, green square). It should be noted that ERA-40 reanalysis budget terms also depend on model parameterizations and are therefore subject to large uncertainties (Back and Bretherton 2005).

TABLE 2. MSE budget terms taken from Eq. (3) (the MSE tendency term is negligible and it is not included). The values are averages over 28°–42°N, 15°–35°E. Each term is also expressed, in parentheses, as a percentage of the MSE divergence, $\langle \omega(\partial m/\partial p)\rangle$.

	$\langle \omega(\partial m/\partial p)\rangle$	$-\langle \mathbf{v}\cdot\nabla c_pT\rangle$	F_{rad}	$-\langle \mathbf{v}\cdot\nabla Lq\rangle$	LHF	SHF
ERA-40	−174.5 (100%)	−224.0 (128%)	−55.8 (32%)	34.3 (−20%)	57.6 (−33%)	36.1 (−21%)
ACCESS1.3	−101.4 (100%)	−103.7 (102%)	−99.4 (98%)	16.8 (−17%)	50.9 (−50%)	27.0 (−27%)
BCC-CSM1.1	−106.3 (100%)	−142.9 (134%)	−82.0 (77%)	22.8 (−21%)	50.9 (−48%)	46.3 (−43%)
CCSM4	−140.7 (100%)	−152.1 (108%)	−98.3 (70%)	26.9 (−19%)	46.9 (−34%)	41.9 (−30%)
CESM1-CAM5	−137.4 (100%)	−145.4 (106%)	−93.3 (68%)	21.9 (−16%)	48.5 (−35%)	42.4 (−31%)
CMCC-CM	−145.0 (100%)	−189.9 (130%)	−68.9 (47%)	46.6 (−32%)	39.0 (−27%)	34.7 (−24%)
CMCC-CMS	−134.7 (100%)	−179.1 (133%)	−65.0 (48%)	32.7 (−24%)	37.4 (−28%)	33.2 (−25%)
CSIRO Mk3.6.0	−119.2 (100%)	−97.8 (82%)	−107.8 (90%)	13.3 (−11%)	41.9 (−35%)	58.6 (−49%)
FGOALS-g2	−137.2 (100%)	−111.7 (81%)	−117.1 (85%)	14.5 (−10%)	51.9 (−38%)	50.3 (−37%)
GFDL CM3	−135.2 (100%)	−182.0 (134%)	−63.2 (61%)	26.6 (−20%)	49.7 (−37%)	40.5 (−30%)
GFDL-ESM2G	−89.6 (100%)	−105.6 (118%)	−80.4 (89%)	16.1 (−18%)	62.7 (−70%)	38.0 (−42%)
HadGEM2-AO	−189.9 (100%)	−198.6 (104%)	−104.4 (55%)	37.4 (−20%)	59.4 (−31%)	37.8 (−20%)
INM-CM4	−106.8 (100%)	−118.7 (111%)	−96.2 (71%)	13.7 (−13%)	22.5 (−21%)	73.4 (−69%)
IPSL-CM5A-MR	−129.5 (100%)	−130.8 (101%)	−109.5 (85%)	22.5 (−17%)	59.6 (−46%)	51.1 (−39%)
MIROC5	−166.9 (100%)	−209.0 (125%)	−103.1 (62%)	45.5 (−27%)	65.8 (−39%)	39.8 (−24%)
MIROC-ESM	−151.4 (100%)	−197.6 (130%)	−106.9 (71%)	19.5 (−13%)	72.2 (−48%)	46.5 (−31%)
MPI-ESM-LR	−199.1 (100%)	−240.3 (121%)	−95.5 (48%)	50.2 (−25%)	62.1 (−31%)	39.8 (−20%)
NorESM1-M	−105.3 (100%)	−134.0 (127%)	−99.2 (94%)	38.7 (−37%)	51.3 (−49%)	42.2 (−40%)

4. The monsoon–desert mechanism at interannual time scales

a. Observations/reanalysis

Following from the results of the previous section, the diversity in the intensity of monsoon heating and associated linear descent response over the Mediterranean implies that year-to-year variations in monsoon intensity, particularly severe weak or strong monsoon years (i.e., 15% of the summer mean climatology), will have an impact on abnormal summer seasonal climate variations over the region (e.g., the 2002 severe drought over India and flood conditions over the European/Mediterranean sectors; Blackburn et al. 2003). The correlation between monsoon rainfall, as measured by all-India rainfall (AIR) index (weighted-area average of rainfall observed over 360 stations distributed over the Indian subcontinent; Parthasarathy et al. 1992), and eastern Mediterranean descent, as measured by area-averaged (28°–42°N, 10°–40°E) omega at 500 hPa, is about 0.48 in the ERA-40 record (44 yr). For the same period, the AIR index, as expected, is negatively but weakly correlated (i.e., −0.26) with the precipitation averaged in the Mediterranean area (EMedpr). Compared to the tropics, the different nature of precipitation in the extratropical regions makes the vertical velocity at 500 hPa a weak proxy for rainfall in those regions. This can explain the lower correlation between AIR and precipitation in the eastern Mediterranean than that with omega. The relative low correlation values suggest also the involvement of other factors, such as the summer North Atlantic Oscillation (NAO; Chronis et al. 2011; Bladé et al. 2012) or blocking events (Blackburn et al. 2003) and related feedbacks, in determining the intensity of Mediterranean summer climate variations. Yet, by focusing only on severe monsoon cases, both in observations and reanalysis (Table 3, years in bold) and CMIP5 model simulations, we try to elucidate if the processes at work at in the time mean are also noticeable at interannual time scales. We performed composite analysis for severe weak and strong monsoon years separately.

Figure 12 shows the composite anomalies of mid-tropospheric omega and precipitation, as well as the leading terms of the MSE equation [Eq. (4)]. The strong monsoon composites (bottom two rows) share large similarities to the summer mean (Fig. 10). The Mediterranean sector experiences much drier and stronger descent conditions during years of severe strong monsoon over South Asia (Fig. 12h). In retrospect, during severe weak monsoon years weaker descent and a slight increase in summer precipitation over Mediterranean are noticeable (Fig. 12c). In both cases, MSE divergence over the Mediterranean is largely balanced by the T_{adv} term (Figs. 12b,g). The F_{rad} anomalies over the Mediterranean are positive during weak monsoon years and they are negative during strong monsoon years (not shown). Enhanced radiative cooling over the eastern Mediterranean during strong monsoon years promotes more descent, favoring drier conditions. The reverse can apply during weak monsoon years. In summary, the monsoon–desert mechanism works at interannual time scales too.

As the changes in T_{adv} dominate anomalous MSE divergence, we decomposed it into various terms [Eq. (5)]. The anomalous horizontal temperature advection is

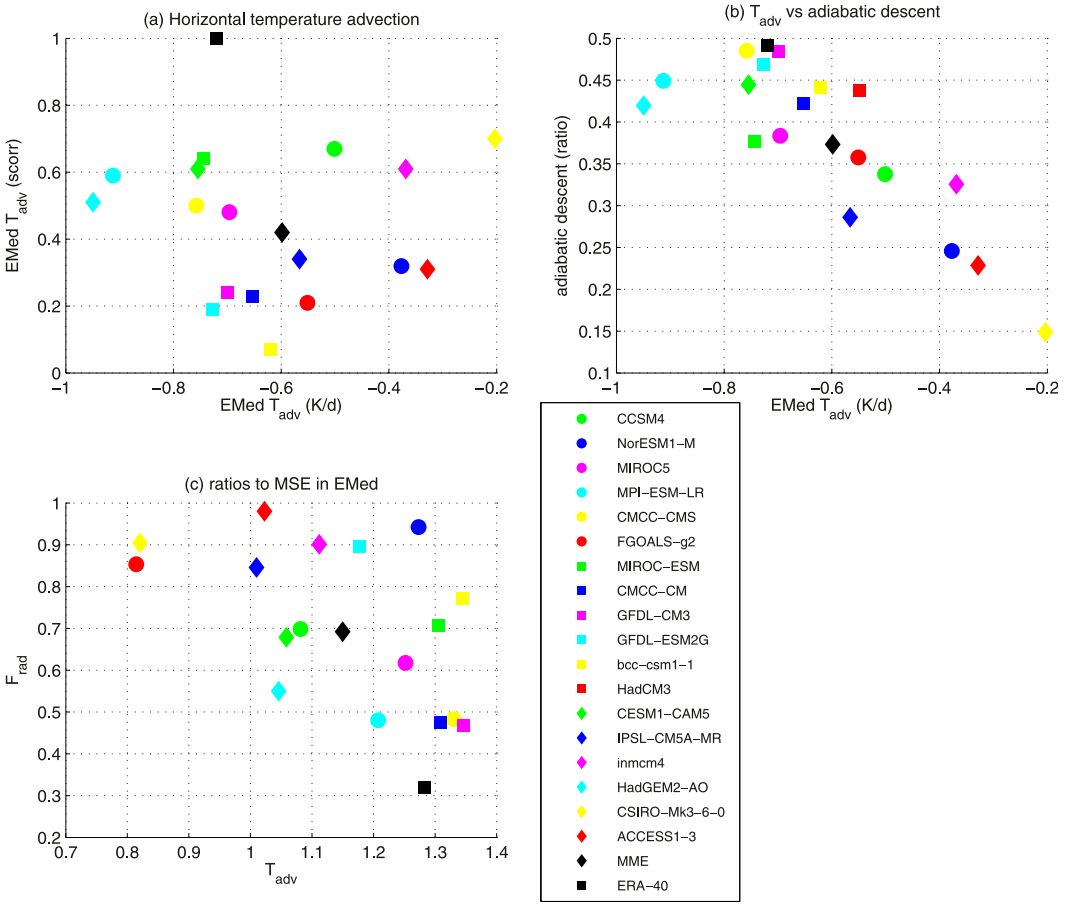

FIG. 11. Scatterplot of horizontal temperature advection (T_{adv}, K day^{-1}) averaged over 28°–42°N, 5°–35°E, vs (a) pattern correlation of the model values with ERA-40 and (b) ratio of adiabatic descent (i.e., ratio between horizontal and vertical temperature advection as absolute value) in the same region. (c) Scatterplot of T_{adv} vs radiative fluxes (F_{rad}) in terms of their contribution to the vertical advection of MSE [see Eq. (3) and Table 2]. The MSE budget values are averaged over 28°–42°N, 15°–35°E.

mostly balanced by the first two terms of Eq. (5) (Figs. 12d,i,e,j), as the other terms are weaker (not shown). In particular, Figs. 12d and 12e (Figs. 12i,j) are the leading contributors to Fig. 12b (Fig. 12g) for weak (strong) monsoon years. Over the region 30°–45°N, 10°–45°E, both the leading terms (Fig. 12d,e) reinforce the total anomalous horizontal temperature advection (Fig. 12b) during weak monsoon years. For the strong monsoon year composite, the anomalous temperature gradient advected by climatological wind (Fig. 12j) contributes more to the weak positive temperature tendency mostly east of 20°E (Fig. 12g). The same composite made considering all the years listed in Table 3 provides similar conclusions, but using only extreme years the anomalies are larger.

b. *CMIP5 simulations*

The sample size used to make composites from observations/reanalysis is small. Therefore, the signals identified there may be influenced by a few strong events. To alleviate this inherent problem, we turn to long integrations made available with CMIP5 models. In this case we need to choose those models that demonstrate realistic teleconnections between the Asian monsoon and the eastern Mediterranean sector. In the models, we measure the intensity of the monsoon with the precipitation anomalies in summer averaged over India (in the area 5°–25°N, 60°–90°E, considering land points only) and we refer to it as Indian monsoon rainfall

TABLE 3. List of strong and weak monsoon years based on standardized AIR index intensity exceeding 1 std for the period 1958–2001. Years in **bold** exceed 1.5 std and they are used for the composite shown in Fig. 12.

Strong monsoon	1959, **1961**, 1970, 1975, 1978, 1980, **1988**, **1994**
Weak monsoon	1962, **1965**, 1966, 1968, **1972**, 1974, **1979**, 1982, 1985, **1987**

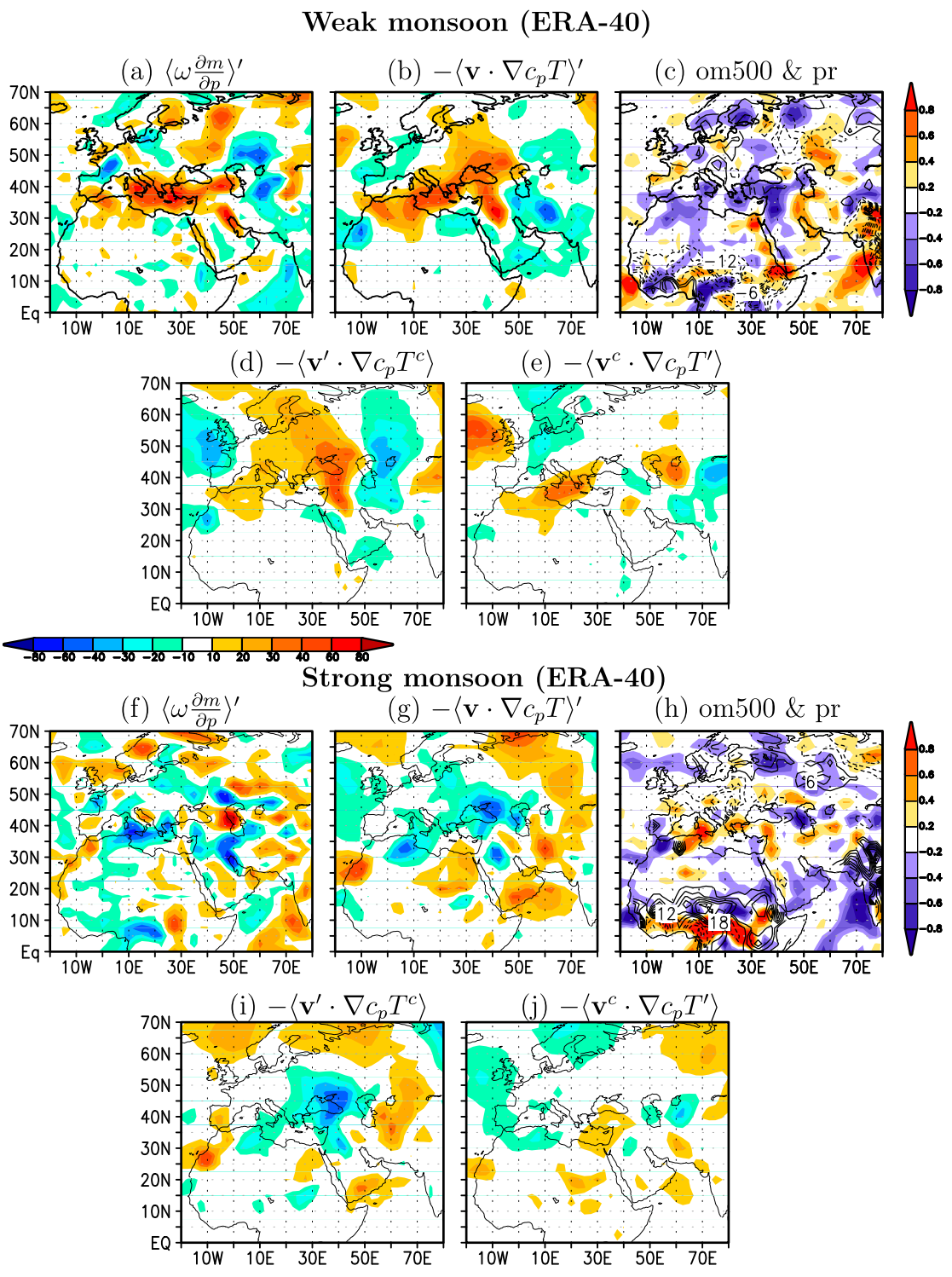

FIG. 12. (top) Weak and (bottom) strong monsoon year composite anomalies of (a),(f) vertical advection of MSE ($\langle\omega(\partial m/\partial p)\rangle$; W m^{-2}), (b),(g) horizontal advection of dry enthalpy ($-\langle\mathbf{v}\cdot\nabla c_pT\rangle$; W m^{-2}), (c),(h) omega at 500 hPa (hPa h^{-1}, shaded), and precipitation (W m^{-2}, contours). Precipitation is measured in W m^{-2} as product of mm day^{-1} and latent heat of vaporization (L), and considering that 1 kg (m^2 day^{-1}) $^{-1}$ equals 1 mm day^{-1}. The other four panels show the first two terms of the horizontal temperature advection decomposition as in Eq. (5): (d),(i) $-\langle\mathbf{v}'\cdot\nabla c_pT^c\rangle$ and (e),(j) $-\langle\mathbf{v}^c\cdot\nabla c_pT'\rangle$ (W m^{-2}). Atmospheric fields are taken from ERA-40 reanalysis, except for precipitation (taken from CRU). Note that (c) and (h) have own palette on the right, while all the other panels share the palette located between the two groups of panels.

TABLE 4. Correlation coefficients between (second column) Indian monsoon rainfall (IMR) index and omega at 500 hPa averaged in the Mediterranean sector (EMedom500), (third column) IMR index and precipitation averaged in the Mediterranean sector (EMedpr), and (fourth column) Niño-3.4 and EMedpr for the CMIP5 models. All the values are computed for JJA. The values in bold are statistically significant at 95%, and the models in bold are the ones selected for the models' composite analysis. IMR is computed from precipitation anomalies averaged over 5°–25°N, 70°–90°E (land points only).

Model	IMR vs EMedom500	IMR vs EMedpr	Niño-3.4 vs EMedpr
ACCESS1.3	0.20	−0.21	**0.39**
BCC-CSM1.1	0.08	−0.11	0.07
CCSM4	0.24	**−0.30**	**0.32**
CESM1-CAM5	**0.32**	−0.15	0.28
CMCC-CM	**0.58**	−0.25	0.21
CMCC-CMS	**0.51**	−0.20	**0.33**
CSIRO Mk3.6.0	0.20	−0.12	0.14
FGOALS-g2	0.28	**−0.41**	0.12
GFDL CM3	**0.45**	−0.05	0.20
GFDL-ESM2G	0.18	−0.02	0.21
HadCM3	**0.32**	−0.10	0.18
HadGEM2-AO	0.19	−0.20	0.14
INM-CM4	0.28	**−0.58**	0.29
IPSL-CM5A-MR	0.02	−0.20	0.12
MIROC5	**0.31**	**−0.30**	**0.49**
MIROC-ESM	0.07	−0.06	0.09
MPI-ESM-LR	0.24	−0.12	0.19
NorESM1-M	0.10	**−0.30**	**0.31**

(IMR) index. Table 4 shows correlation coefficients computed between IMR and omega at 500 hPa and precipitation both averaged in the Mediterranean region (EMedom500 and EMedpr, respectively) in the CMIP5 models' historical simulations. In most models, correlation coefficients are nonsignificant or weaker than observed (Table 4, statistically significant values are bold highlighted).

At interannual time scales, there exists a negative relationship between South Asian summer monsoon rainfall and ENSO indices (Walker and Bliss 1932; Cherchi and Navarra 2013, among others). In retrospect, correlation between summer EMedpr and tropical eastern Pacific SST is positive (not shown). For instance, in the observations the correlation coefficient between Niño-3.4 and EMedpr is 0.34. The corresponding values for the CMIP5 models are reported in Table 4. Based on this interlinked relationship among ENSO, monsoon rainfall, and Mediterranean descent/rainfall, we selected three models (highlighted in bold in Table 4) for further analysis. These models are MIROC5, CCSM4, and NorESM1-M. In each of these models, severe weak and strong monsoon years are identified when the IMR index exceeds 1.5 standard deviations (std; e.g., combining the three models we counted a total of 18 strong and 19 weak monsoon years), and then a multimodel mean composite analysis is performed and the results are shown in Fig. 13.

To make direct comparison with the reanalysis (Fig. 12), Fig. 13 shows the same variables from the multimodel mean composites taken from the three selected models. On the large scale, the model composites agree with the reanalysis showing positive (negative) values in MSE divergence over the Mediterranean (Figs. 13a,f), associated with positive (negative) T_{adv} (Figs. 13b,g) during weak (strong) monsoon years. In the models these features are distorted by noisy variables like omega and precipitation. However, even if the anomalies of omega and precipitation are weak (Figs. 13c,h), they are statistically significant and indicative of enhanced (decreased) rainfall and anomalous ascent (descent) during weak (strong) monsoon years, consistent with the results from reanalysis. Even in the models, T_{adv} dominates the MSE budget (Figs. 13a,b,f,g). Partitioning the anomalous horizontal temperature advection in the models' composites shows that the leading terms agree with that from the reanalysis (Figs. 13d,e,j,i). One systematic model error is that in strong monsoon cases, the contribution by the climatological wind advecting anomalous temperature (Figs. 13j) is larger than noted in the reanalysis (Figs. 12j). Overall, MSE budget terms from CMIP5 models' composites mostly agree with those identified with reanalysis.

c. *El Niño sensitivity experiments*

To strengthen the above results, we diagnosed MSE budget terms in an existing ensemble of AM2.1 sensitivity experiments (section 2a), and the results are summarized in Fig. 14. In response to El Niño forcing, rainfall anomalies are negative over South Asia (Fig. 14a) and the vertical structure of omega averaged over the

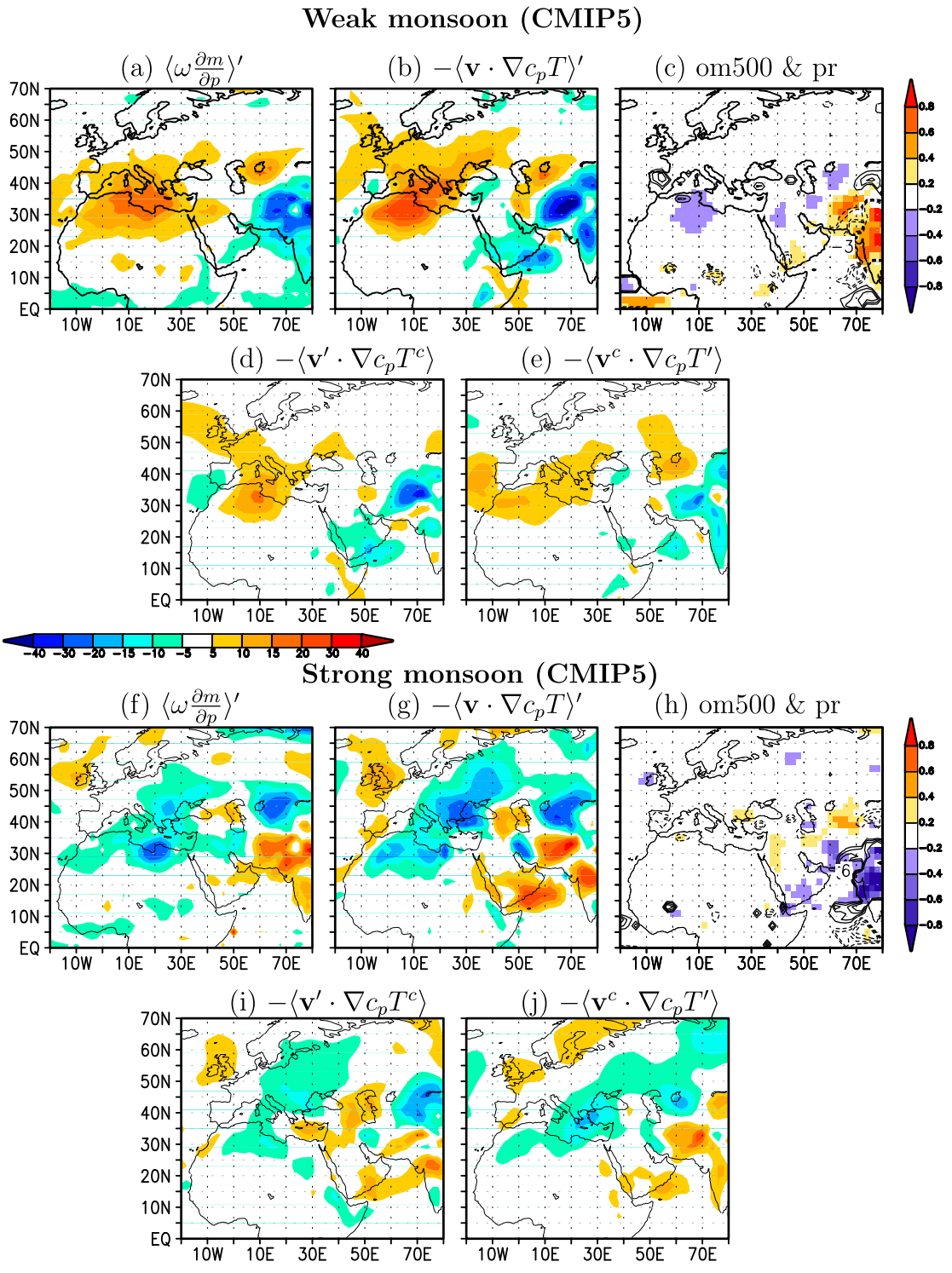

FIG. 13. As in Fig. 12, but for the composite computed from MIROC5, NorESM1-M, and CCSM4 experiments. In (c) and (h) only the values statistically significant (95% level) are shown. The composites are tested for statistical significance with a nonparametric test using resampling technique (Cherchi et al. 2014).

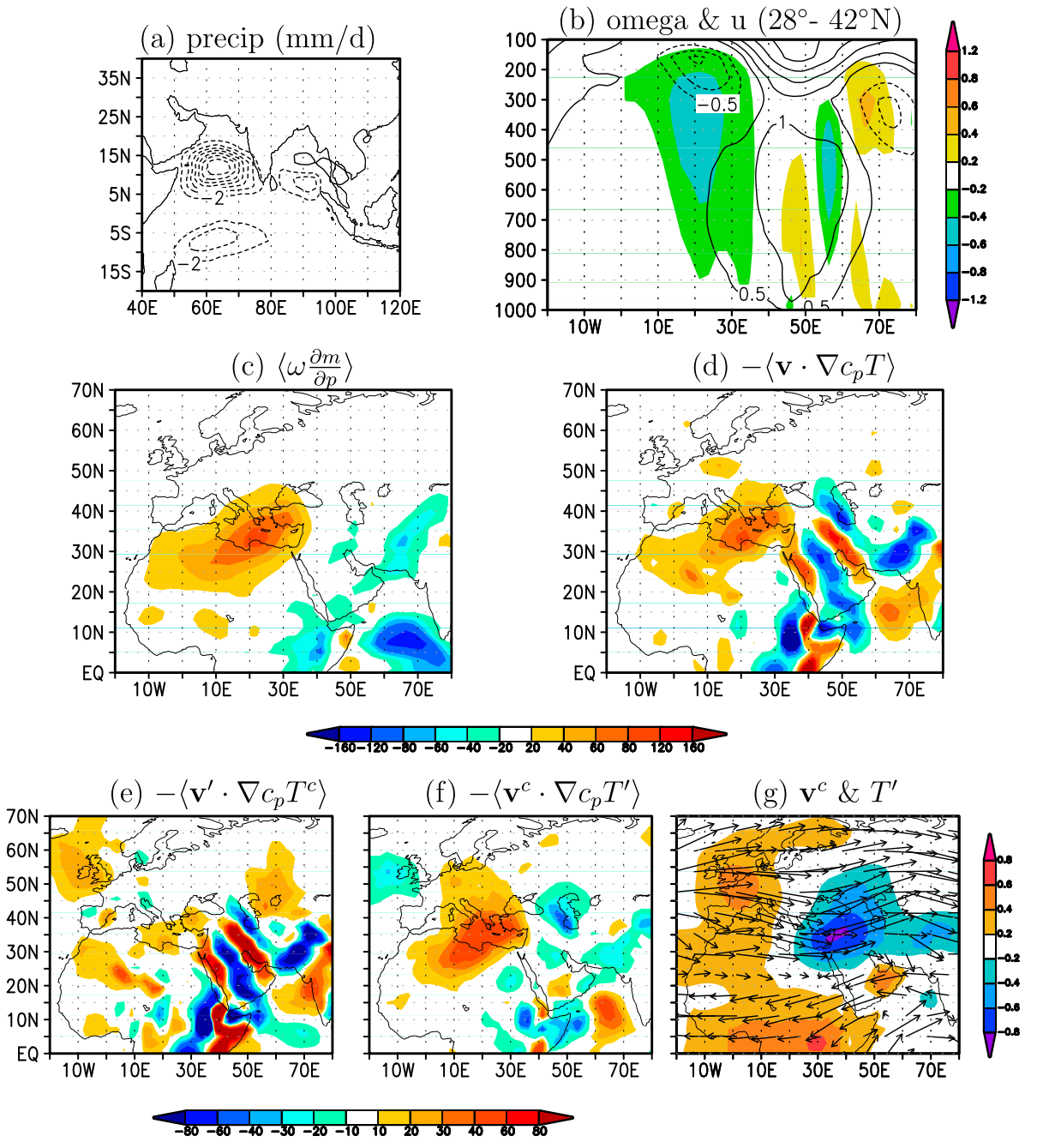

FIG. 14. JJA mean differences (El Niño sensitivity experiments) of (a) precipitation (mm day^{-1}), (b) vertical profile of omega (hPa h^{-1}, shaded) and zonal wind (m s^{-1}, contours) averaged over 28°–42°N, (c) vertical advection of MSE ($\langle\omega(\partial m/\partial p)\rangle$; W m^{-2}), (d) horizontal advection of dry enthalpy ($-\langle\mathbf{v}\cdot\nabla c_pT\rangle$; W m^{-2}), (e),(f) first two terms of the decomposition of anomalous horizontal temperature advection (in W m^{-2}), $-\langle\mathbf{v}'\cdot\nabla c_pT^c\rangle$ and $-\langle\mathbf{v}^c\cdot\nabla c_pT'\rangle$, respectively, and (g) vertically averaged climatological wind (m s^{-1}, vectors) and anomalous temperature (K, shaded).

Mediterranean latitudes is of anomalous ascent (Fig. 14b). Regarding the budget, while the major results (Figs. 14c,d) are consistent with those of the reanalysis (Fig. 12) and CMIP5 models (Fig. 13), climatological wind advecting the anomalous temperature gradient (Fig. 14f) dominates the total T_{adv} (Fig. 14d). The reason is that climatological midtropospheric westerlies when deflecting northerly (Ben-Gai et al. 2001) are efficient in advecting warm temperature from the African–Atlantic sectors (Fig. 14g). The complex anomalous meridional wind (Pillai and

Annamalai 2012) largely accounts for the finer-scale features in T_{adv} over the Arabian Peninsular regions (Fig. 14e).

In summary, our results based on reanalysis, on CMIP5 models that best represent the interlinkages among ENSO, monsoon rainfall, and the Mediterranean descent/rainfall, and on an idealized sensitivity experiment with an AGCM provide evidence that the monsoon–desert mechanism works at interannual time scales, particularly for severe weak and strong monsoon years. At interannual time scales there are more competing factors at play, and it is more difficult to give a clear interpretation as in the summer mean case. Despite that, we have been able to show that most of the processes identified for the summer mean are at work also at interannual time scales. The evidence is in agreement with the overall budget diagnostics.

5. Summary and discussion

a. Summary

The availability of multicentury-long integrations with a suite of state-of-the-art coupled climate models provided a unique opportunity to examine the ability of these models in representing the ''monsoon–desert mechanism'' and the relevant physical processes involved in this teleconnection. A systematic evaluation is performed of the CMIP5 capability to resolve the major aspects of this teleconnections, such as 1) the position and intensity of monsoon rainfall and vertical distribution of the associated diabatic heating; 2) midlatitude flow crossing 325-K isentropic surfaces and the northerly wind component in the desert-descent region; and 3) contributions by horizontal temperature advection and net radiative flux. The CMIP5 results are compared to the reanalysis depiction of these mechanisms. Both statistical metrics and solutions from a linear atmosphere model are analyzed, in addition to performing a detailed moist static energy (MSE) budget. We examined the teleconnection both in the summer mean climatology as well as at interannual time scales.

Despite a large spatial diversity in the precise location of simulated South Asian summer monsoon rainfall and associated diabatic heating, we note a linear relationship between the intensities of Q_v and descent over the eastern Mediterranean. The models in which the monsoon is virtually absent depict the weakest midlatitude winds and minimum descent over the Mediterranean, as well as little vertical variation in Q_p. Linear model solutions forced with diabatic heating that mimics the summer mean rainfall simulated by CMIP5 models suggest that the combined diabatic heating pattern over the Arabian Sea/Bay of Bengal regions exerts the largest descent over the eastern Mediterranean. In response to heating centered either in the equatorial Indian Ocean or only over the Arabian Sea region, remote descent of varying intensities is simulated. Equatorially trapped Rossby waves emanating from the monsoon region force the descent over the Mediterranean. Whereas most CMIP5 models simulate descent over the Mediterranean, there is large spread in the location of simulated rainfall associated with the monsoon.

In the models, the MSE budget analysis revealed that horizontal temperature advection represents the main balance with the vertical advection of MSE, consistent with reanalysis. On the other hand, the models tend to underestimate the contribution due to adiabatic descent while overestimating the contribution from radiative cooling, suggesting that local diabatic enhancement in the models may play a more important role in determining the intensity of the descent. We note that ERA-40 reanalysis budget terms also depend on inherent model parameterizations and they are therefore subject to large uncertainties.

In the summer mean climatology our diagnostics identify only a few CMIP5 models that capture the monsoon–desert mechanism for the correct reasons. The model identification is supported by convergent statistical measures and budget diagnostics. Further, we found the same physical processes at interannual time scales, both in reanalysis/observations and in some CMIP5 models. In fact, despite some differences and the intrinsic difficulties in the analysis of the variability because there are more competing factors at work, we have been able to relate results from observations/reanalysis and selected CMIP5 models, as well as from weak monsoon (i.e., El Niño) sensitivity experiments. The differences, found mostly comparing the decomposition of the horizontal temperature advection in models and reanalysis, could have many origins, including systematic errors in the models. In this framework, we cannot exclude that the results of the reanalysis may be influenced by the small sample of cases available. The subset of models identified here is being evaluated for future projections of summer-mean climate and its variability over the Mediterranean. Apart from the discussed mechanism, in CMIP5 simulations large values of radiative flux and its overestimated contribution to the MSE budget interact with other mechanisms, as listed in the introduction, triggering the descent over the eastern Mediterranean. Some caveats and implications of the present study are discussed next.

b. Discussion

To represent the monsoon–desert mechanism, coupled models must capture the main ingredients:

monsoon-associated deep convection and latent heat release. While models have steadily improved in simulating the monsoon, large systematic errors persist (Sperber et al. 2013). To realistically simulate the monsoon rainfall and its vertical distribution of diabatic heating and MSE, challenging tasks include parameterizations of cumulus convection, clouds, and radiation, and their interactions. For example, the model-simulated vertical profiles of diabatic heating over South Asia, compared to reanalysis profiles, tend to have more heating in the lower troposphere (900–700 hPa) and less heating in the upper layers (700–300 hPa). It is unclear if shallow to deep convection processes are adequately represented in the models. Similarly, the simulated larger contribution to MSE vertical advection by diabatic descent (i.e., through radiative cooling) rather than by adiabatic descent, which we have shown in the Mediterranean, calls for systematic errors in cloud–radiative processes.

In our picture the midlatitude dynamics interact with the circulation in the eastern Mediterranean because of the role of midtropospheric northerly wind in promoting descent in the region. By analyzing CMIP5 in the Mediterranean, we showed a relationship between the underestimation of the northerly wind velocity in the midtroposphere and the intensity of local descent. To complete the discussion it is worth mentioning that the Mediterranean climate is influenced also by other midlatitudes processes. A positive phase of the summer NAO provides strong anticyclonic flow and suppressed precipitation over the United Kingdom, but anomalous wet conditions in the Mediterranean region (Bladé et al. 2012). Blocking high pressure systems over Europe sometimes sustain similar conditions diverting the jet stream to the north or south (Blackburn et al. 2003). Even in this picture, model weaknesses resolving the summer NAO, as for example identified in CMIP3 (Bladé et al. 2012), would affect the simulated climate in the eastern Mediterranean.

The diagnostics presented here provide guidance for model developments, although sustained three-dimensional observations of moisture and cloud–radiative processes are necessary to more precisely constrain model simulations of the monsoon. When these processes and associated feedbacks are not well represented, the model biases compromise performance of simulated large-scale teleconnections, such as the monsoon–desert mechanism.

Acknowledgments. We acknowledge the World Climate Research Programme's Working Group on Coupled Modeling, which is responsible for CMIP, and we thank the climate modeling groups (listed in Table 1 of this paper) for producing and making available their model outputs. For CMIP the U.S. Department of Energy's Program for Climate Model Diagnosis and Intercomparison provides coordinating support and led development of software infrastructure in partnership with the Global Organization for Earth System Science Portals. The financial support of the Italian Ministry of Education, University and Research, and Ministry for Environment, Land and Sea through the project GEMINA and that of INDO-MARECLIM (Project 295092) is gratefully acknowledged. A. Cherchi thankfully acknowledges the generous hospitality of the International Pacific Research Center at UH Manoa, Honolulu. Jan Hafner is thanked for providing the moist static energy budget code used here and Matthew Windlansky is thanked for comments and proof reading. H. Annamalai acknowledges the partial support by the Office of Science (BER) U.S. Department of Energy, Grant DE-FG02-07ER6445, and also by the three institutional grants (JAMSTEC, NASA, NOAA) of the IPRC. Dr. Chen and an anonymous reviewer are acknowledged for the instructive and helpful comments given.

REFERENCES

Adler, R. F., and Coauthors, 2003: The Version-2 Global Precipitation Climatology Project (GPCP) monthly precipitation analysis (1979–present). *J. Hydrometeor.,* **4,** 1147–1167, doi:10.1175/1525-7541(2003)004<1147:TVGPCP>2.0.CO;2.

Ananthakrishnan, R., J. Pathan, and S. Aralikati, 1983: The onset phase of the southwest monsoon. *Curr. Sci.,* **52,** 755–764.

Anderson, J., and Coauthors, 2004: The new GFDL global atmosphere and land model AM2-LM2: Evaluation with prescribed SST simulations. *J. Climate,* **17,** 4641–4673, doi:10.1175/JCLI-3223.1.

Annamalai, H., 2010: Moist dynamical linkage between the equatorial Indian Ocean and the South Asian monsoon trough. *J. Atmos. Sci.,* **67,** 589–610, doi:10.1175/2009JAS2991.1.

——, and K. Sperber, 2005: Regional heat sources and the active and break phases of boreal summer intraseasonal (30–50 day) variability. *J. Atmos. Sci.,* **62,** 2726–2748, doi:10.1175/JAS3504.1.

——, J. Hafner, K. Sooraj, and P. Pillai, 2013: Global warming shifts the monsoon circulation, drying South Asia. *J. Climate,* **26,** 2701–2718, doi:10.1175/JCLI-D-12-00208.1.

Back, L., and C. Bretherton, 2005: The relationship between wind speed and precipitation in the Pacific ITCZ. *J. Climate,* **18,** 4317–4328, doi:10.1175/JCLI3519.1.

Ben-Gai, T., A. Bitan, A. Manes, P. Alpert, and Y. Kushnir, 2001: Temperature and surface pressure anomalies in Israel and the North Atlantic Oscillation. *Theor. Appl. Climatol.,* **69,** 171–177, doi:10.1007/s007040170023.

Blackburn, M., B. Hoskins, P. Inness, and J. Slingo, 2003: 2002—A summer of floods and drought. *Planet Earth,* summer 2003 issue, Natural Environment Research Council, Swindon, United Kingdom, 23.

Bladé, I., B. Liebmann, D. Fortuny, and G. van Oldenborgh, 2012: Observed and simulated impact of the summer NAO in Europe: Implications for projected drying in the Mediterranean region. *Climate Dyn.,* **39,** 709–727, doi:10.1007/s00382-011-1195-x.

Boos, W., and J. Hurley, 2013: Thermodynamic bias in the multimodel mean boreal summer monsoon. *J. Climate,* **26,** 2279–2287, doi:10.1175/JCLI-D-12-00493.1.

Charney, J., 1975: Dynamics of deserts and drought in the Sahel. *Quart. J. Roy. Meteor. Soc.,* **101,** 193–202, doi:10.1002/qj.49710142802.

Chen, J., and S. Bordoni, 2014a: Orographic effects of the Tibetan Plateau on the East Asian summer monsoon: An energetic perspective. *J. Climate,* **27,** 3052–3072, doi:10.1175/JCLI-D-13-00479.1.

——, and ——, 2014b: Intermodel spread of East Asian summer monsoon simulations in CMIP5. *Geophys. Res. Lett.,* **41,** 1314–1321, doi:10.1002/2013GL058981.

Chen, P., M. Hoerling, and R. Dole, 2001: The origin of the subtropical anticyclones. *J. Atmos. Sci.,* **58,** 1827–1835, doi:10.1175/1520-0469(2001)058<1827:TOOTSA>2.0.CO;2.

Cherchi, A., and A. Navarra, 2013: Influence of ENSO and of the Indian Ocean dipole on the Indian summer monsoon variability. *Climate Dyn.,* **41,** 81–103, doi:10.1007/s00382-012-1602-y.

——, A. Carril, C. Menéndez, and L. Zamboni, 2014: La Plata Basin precipitation variability in spring: Role of remote SST forcing as simulated by GCM experiments. *Climate Dyn.,* **42,** 219–236, doi:10.1007/s00382-013-1768-y.

Chou, C., and J. Neelin, 2003: Mechanisms limiting the northward extent of the northern summer monsoons over North America, Asia and Africa. *J. Climate,* **16,** 406–425, doi:10.1175/1520-0442(2003)016<0406:MLTNEO>2.0.CO;2.

Chronis, T., D. Raitsos, D. Kassis, and A. Sarantopoulos, 2011: The summer North Atlantic Oscillation influence on the eastern Mediterranean. *J. Climate,* **24,** 5584–5596, doi:10.1175/2011JCLI3839.1.

Dai, A., 2006: Precipitation characteristics in eighteen coupled climate models. *J. Climate,* **19,** 4605–4630, doi:10.1175/JCLI3884.1.

Delworth, T., and Coauthors, 2006: GFDL's CM2 global coupled climate models. Part I: Formulation and simulation characteristics. *J. Climate,* **19,** 643–674, doi:10.1175/JCLI3629.1.

Gaetani, M., B. Pohl, H. Douville, and B. Fontaine, 2011: West African monsoon influence on the summer Euro-Atlantic circulation. *Geophys. Res. Lett.,* **38,** L09705, doi:10.1029/2011GL047150.

Giorgi, F., and P. Lionello, 2008: Climate change projections for the Mediterranean region. *Global Planet. Change,* **63,** 90–104, doi:10.1016/j.gloplacha.2007.09.005.

Hoskins, B., 1996: On the existence and strength of the summer subtropical anticyclones – Bernhard Haurwitz Memorial. *Bull. Amer. Meteor. Soc.,* **77,** 1287–1292.

——, and B. Wang, 2006: Large-scale atmospheric dynamics. *The Asian Monsoon,* B. Wang, Ed., Springer, 357–415.

——, H. Hsu, I. James, M. Masutani, P. Sardeshmukh, and G. White, 1989: Diagnostics of the global atmospheric circulation based on ECMWF analysis 1979–1989. WCRP-27, WMO/TD-326, 217 pp.

Kalnay, E., and Coauthors, 1996: The NCEP/NCAR 40-Year Reanalysis Project. *Bull. Amer. Meteor. Soc.,* **77,** 437–471, doi:10.1175/1520-0477(1996)077<0437:TNYRP>2.0.CO;2.

Kiranmayi, L. and E. Maloney, 2011: Intraseasonal moist static energy budget in reanalysis data. *J. Geophys. Res.,* **116,** D21117, doi:10.1029/2011JD016031.

Lionello, P., and Coauthors, 2006: Cyclones in the Mediterranean region: Climatology and effects on the environment. *Mediterranean Climate Variability,* P. Lionello, P. Malanotte-Rizzoli, and R. Boscolo, Eds., Elsevier, 27–148.

Liu, Y., G. Wu, and R. Ren, 2004: Relationship between the subtropical anticyclone and diabatic heating. *J. Climate,* **17,** 682–698, doi:10.1175/1520-0442(2004)017<0682:RBTSAA>2.0.CO;2.

Mariotti, A., M. Struglia, N. Zeng, and K.-M. Lau, 2002: The hydrological cycle in the Mediterranean region and implications for the water budget of the Mediterranean Sea. *J. Climate,* **15,** 1674–1690, doi:10.1175/1520-0442(2002)015<1674:THCITM>2.0.CO;2.

Mitchell, T., and P. Jones, 2005: An improved method of constructing a database of monthly climate observations and associated high-resolution grids. *Int. J. Climatol.,* **25,** 693–712, doi:10.1002/joc.1181.

Nakamura, H., and T. Miyasaka, 2004: Formation of summertime subtropical highs. *Bull. Amer. Meteor. Soc.,* **85,** 1062–1064.

Neelin, J., 2007: Moist dynamics of tropical convection zones in monsoons, teleconnections, and global warming. *The Global Circulation of the Atmosphere,* T. Schneider and A. Sobel, Eds., Princeton University Press, 267–301.

Nigam, S., C. Chung, and E. DeWeaver, 2000: ENSO diabatic heating in ECMWF and NCEP–NCAR reanalyses, and NCAR CCM3 simulation. *J. Climate,* **13,** 3152–3171, doi:10.1175/1520-0442(2000)013<3152:EDHIEA>2.0.CO;2.

Parthasarathy, B., A. Munot, and D. Kothwale, 1992: Indian summer monsoon rainfall indices: 1871–1990. *Meteor. Mag.,* **121,** 174–186.

Pillai, P., and H. Annamalai, 2012: Moist dynamics of severe monsoons over South Asia: Role of the tropical SST. *J. Atmos. Sci.,* **69,** 97–115, doi:10.1175/JAS-D-11-056.1.

Prasanna, V., and H. Annamalai, 2012: Moist dynamics of extended monsoon breaks over South Asia. *J. Climate,* **25,** 3810–3831, doi:10.1175/JCLI-D-11-00459.1.

Raicich, F., N. Pinardi, and A. Navarra, 2003: Teleconnections between Indian monsoon and Sahel rainfall and the Mediterranean. *Int. J. Climatol.,* **23,** 173–186, doi:10.1002/joc.862.

Rodwell, M., and B. Hoskins, 1996: Monsoons and the dynamics of deserts. *Quart. J. Roy. Meteor. Soc.,* **122,** 1385–1404, doi:10.1002/qj.49712253408.

——, and ——, 2001: Subtropical anticyclones and summer monsoons. *J. Climate,* **14,** 3192–3211, doi:10.1175/1520-0442(2001)014<3192:SAASM>2.0.CO;2.

Schumacher, C., R. A. Houze Jr., and I. Kraucunas, 2004: The tropical dynamical response to latent heating estimates derived from the TRMM precipitation radar. *J. Atmos. Sci.,* **61,** 1341–1358, doi:10.1175/1520-0469(2004)061<1341:TTDRTL>2.0.CO;2.

Seager, R., R. Murtugudde, N. Naik, A. Clement, N. Gordon, and J. Miller, 2003: Air–sea interaction and the seasonal cycle of the subtropical anticyclones. *J. Climate,* **16,** 1948–1966, doi:10.1175/1520-0442(2003)016<1948:AIATSC>2.0.CO;2.

Sperber, K., H. Annamalai, I. Kang, A. Kitoh, A. Moise, A. Turner, B. Wang, and T. Zhou, 2013: The Asian summer monsoon: An intercomparison of CMIP5 vs CMIP3 simulations of the late 20th century. *Climate Dyn.,* **41,** 2711–2744, doi:10.1007/s00382-012-1607-6.

Su, H., and J. Neelin, 2002: Teleconnection mechanisms for tropical Pacific descent anomalies during El Niño. *J. Atmos. Sci.,* **59,** 2694–2712, doi:10.1175/1520-0469(2002)059<2694:TMFTPD>2.0.CO;2.

Taylor, K., R. Stouffer, and G. Meehl, 2012: An overview of CMIP5 and the experiment design. *Bull. Amer. Meteor. Soc.,* **93,** 485–498, doi:10.1175/BAMS-D-11-00094.1.

Tyrlis, E., J. Lelieveld, and B. Steil, 2013: The summer circulation over the eastern Mediterranean and the Middle East: Influence of the South Asian monsoon. *Climate Dyn.,* **40,** 1103–1123, doi:10.1007/s00382-012-1528-4.

Uppala, S., and Coauthors, 2005: The ERA-40 Re-Analysis. *Quart. J. Roy. Meteor. Soc.,* **131,** 2961–3012, doi:10.1256/qj.04.176.

Walker, G., and E. Bliss, 1932: World Weather V. *Mem. Roy. Meteor. Soc.,* **4,** 53–84.

Watanabe, M., and M. Kimoto, 2000: Atmosphere–ocean thermal coupling in the North Atlantic: A positive feedback. *Quart. J. Roy. Meteor. Soc.,* **126,** 3343–3369, doi:10.1002/qj.49712657017; Corrigendum, **127,** 733–734, doi:10.1002/qj.49712757223.

——, and F. Jin, 2002: Role of Indian Ocean warming in the development of Philippine Sea anticyclone during ENSO. *Geophys. Res. Lett.,* **29,** doi:10.1029/2001GL014318.

Wu, Z., E. Sarachik, and D. Battisti, 2000: Vertical structure of convective heating and the three-dimensional structure of the forced circulation on an equatorial beta plane. *J. Atmos. Sci.,* **57,** 2169–2187, doi:10.1175/1520-0469(2000)057<2169:VSOCHA>2.0.CO;2.

Xie, P., J. Janowiak, P. Arkin, R. Adler, A. Gruber, R. Ferraro, G. Huffmann, and S. Curtis, 2003: GPCP pentad precipitation analyses: An experimental dataset based on gauge observations and satellite estimates. *J. Climate,* **16,** 2197–2214, doi:10.1175/2769.1.

Ziv, B., H. Saaroni, and P. Alpert, 2004: The factors governing the summer regime of the eastern Mediterranean. *Int. J. Climatol.,* **24,** 1859–1871, doi:10.1002/joc.1113.